

The Morphology of Reionization in a Dynamically Clumpy Universe

Christopher Cain,¹  Anson D'Aloisio,¹ Nakul Gangolli¹ and Matthew McQuinn²

¹Department of Physics and Astronomy, University of California, Riverside, CA 92521, USA

²Department of Astronomy, University of Washington, Seattle, WA 98195-1580, USA

Accepted XXX. Received YYY; in original form ZZZ

arXiv:2207.11266v1 [astro-ph.CO] 22 Jul 2022

ABSTRACT

A recent measurement of the Lyman-limit mean free path at $z = 6$ suggests it may have been very short, motivating a better understanding of the role that ionizing photon sinks played in the reionization process. Accurately modeling the sinks in reionization simulations is challenging because of the large dynamic range required if gas structures on scales $\sim 10^4 - 10^8 M_\odot$ contributed significant opacity. As a result, there is no consensus on how important the sinks were in shaping reionization's morphology and its observables. We address this question with a recently developed radiative transfer code that includes a dynamical sub-grid model for the sinks based on radiative hydrodynamics simulations. Compared to assuming a fully pressure-smoothed IGM, our dynamical treatment reduces the predicted sizes of ionized bubbles by 10 – 20% under typical assumptions about reionization's sources. Near the midpoint of reionization, the 21 cm power at $k \sim 0.1 h\text{Mpc}^{-1}$ is reduced by a similar factor. These effects are more modest than the 25 – 45% power suppression resulting from the much higher recombination rate in models that neglect pressure smoothing entirely. Whether the sinks played a significant role in reionization's morphology depends on the nature of its sources. For example, if reionization was driven by bright ($M_{\text{UV}} < -17$) galaxies, the sinks reduce the large-scale 21 cm power by at most 15%, even if pressure smoothing is neglected. Conveniently, when bright sources contribute significantly, the morphology in our dynamical treatment can be reproduced to high accuracy with a uniform sub-grid clumping factor that yields the same ionizing photon budget. By contrast, if $M_{\text{UV}} \sim -13$ galaxies drove reionization, an accurate model of the sinks' dynamics is more important, with the uniform clumping model erring at the 20% level.

Key words: keyword1 – keyword2 – keyword3

1 INTRODUCTION

The past decade has seen an increase in the number and quality of observational constraints on the Epoch of Reionization (EoR). Planck's measurement of the cosmic microwave background (CMB) Thomson scattering optical depth (τ_{es}) have revised the midpoint of reionization to $z \approx 7.5$, driving the field toward late reionization models (Planck Collaboration et al. 2020). Meanwhile, studies of damping wings in high-z quasar spectra (Mortlock et al. 2011; Greig et al. 2016; Davies et al. 2018) and Lyman Alpha Emitter (LAE) surveys (Kashikawa et al. 2006; Ono et al. 2011; Schenker et al. 2012; Pentericci et al. 2014; Mesinger et al. 2015; Ouchi et al. 2018; Hu et al. 2019) have also suggested a significantly neutral intergalactic medium (IGM) at $z \sim 7$. At $z \lesssim 6$, quasar absorption spectra measurements may also be consistent with an ongoing reionization process down to $z \sim 5$ (e.g. Fan et al. 2006; Becker et al. 2015; Bosman et al. 2018; Eilers et al. 2018; Kulkarni et al. 2019; Keating et al. 2020b; Nasir & D'Aloisio 2020; Qin et al. 2021; Becker et al. 2021; Cain et al. 2021; Bosman et al. 2021; Zhu et al. 2021). Future observations with the James Webb Space Telescope (JWST), the extremely large telescopes, 21 cm signal experiments – e.g. SKA (Mellema et al. 2013) and HERA (Abdurashidova et al. 2022a,b) – and other line intensity mapping surveys (e.g. SPHEREx; Doré et al. 2014), promise to vastly expand our understanding of the EoR. This

wealth of forthcoming data motivates theoretical studies to predict and interpret reionization observables with greater accuracy.

All reionization observables, with the exception of τ_{es} , are sensitive to the spatial structure of ionized regions, broadly termed morphology. Reionization's morphology is known to be sensitive to the nature of its sources as well as the LyC opacity of the IGM (Furlanetto & Oh 2005; Iliev et al. 2005b; McQuinn et al. 2007; Alvarez & Abel 2012; Sobacchi & Mesinger 2014; Davies & Furlanetto 2022). During reionization, gaseous halos with masses $\lesssim 10^8 M_\odot$, which are too small to form stars, act as sinks of ionizing photons and play a role in setting the IGM opacity (Shapiro et al. 2004; Iliev et al. 2005b). The sinks can be as small as $10^4 M_\odot$ before reionization, roughly the Jeans filtering scale in the cold IGM (Gnedin 2000; Naoz & Barkana 2007; Emberson et al. 2013). Once the IGM surrounding these structures ionizes, their gas is photo-evaporated and pressure-smoothed over a timescale of a few hundred Myr (Iliev et al. 2005a; Park et al. 2016; D'Aloisio et al. 2020; Nasir et al. 2021). We refer to this process as relaxation. Modeling relaxation in simulations requires high ($\sim \text{kpc}$) spatial resolution to resolve the sinks (Emberson et al. 2013) and radiative transfer (RT) coupled to the hydrodynamics to capture the interplay between self-shielding and pressure smoothing (Park et al. 2016; D'Aloisio et al. 2020).

In RT simulations that are big enough to capture the large-scale structure of patchy reionization ($\gtrsim 200$ –300 Mpc, Iliev et al. 2014; Kaur et al. 2020), resolving the sinks presents an extreme computational challenge owing to the > 5 orders of magnitude in spatial

* E-mail: ccain002@ucr.edu

scales that are required. RT simulations that come close (e.g. [Gnedin 2014](#); [Ocvirk et al. 2016](#); [Kannan et al. 2022](#)) are too expensive to run more than a handful of times. On the other hand, the semi-numerical methods of approximating RT that have been employed for parameter space studies either ignore the effect of the sinks or model them in an approximate manner (e.g. [Choudhury et al. 2021](#); [Gazagnes et al. 2021](#); [Davies & Furlanetto 2022](#)). It is unclear, however, which approximation schemes for the sinks are accurate. Simulations that ignore the unresolved sinks implicitly assume that their effects are fully degenerate with the parameters that characterize the sources ([Iliev et al. 2005b](#)). Other studies have attempted to model unresolved sinks with a sub-grid clumping factor ([McQuinn et al. 2007](#); [Mao et al. 2020](#)), by adding extra opacity to their cells ([Shukla et al. 2016](#); [Giri et al. 2019a](#)), or by specifying the mean free path as an input ([Davies & Furlanetto 2016](#); [Wu et al. 2022](#); [Davies & Furlanetto 2022](#); [Trac et al. 2022](#)). These implementations vary in complexity and often disagree on what role the sinks play. As a result, currently there is no consensus on how much of an effect the sinks have on reionization and, relatedly, how important they are for interpreting observables. This paper aims to further address these questions.

Another motivation for the current study is the recent measurement of the Lyman-Limit mean free path at $z = 6$ by [Becker et al. 2021](#) (see also [Bosman 2021](#) for complementary constraints). They reported a value of $\lambda_{912}^{\text{mfp}} = 3.57^{+3.09}_{-2.14} h^{-1} \text{cMpc}$, which is considerably shorter than extrapolations from measurements at lower redshift ([Worseck et al. 2014](#)). In addition to suggesting that the IGM may have still been significantly neutral at $z = 6$ ([Cain et al. 2021](#); [Garaldi et al. 2022](#); [Lewis et al. 2022](#)), their measurement – if confirmed – may indicate that absorptions in ionized gas consumed a majority of the reionization photon budget ([Davies et al. 2021](#)); in which case, accounting for the effect of sinks in simulations would be critical.

The main goal of this work is to assess how important the sinks are for modeling reionization’s morphology. Towards this end, we use a new ray-tracing RT code that was first applied in [Cain et al. \(2021\)](#). The code has been developed for flexibility and low computational cost, mainly by the use of large cell sizes and adjustable angular resolution in the RT calculation. For our fiducial simulations, we employ the [Cain et al. \(2021\)](#) sub-grid model based on a suite of high-resolution, fully coupled hydro/RT simulations, which track how the LyC opacity of the IGM evolves in different environments after I-fronts sweep through (an expanded version of the numerical experiments in [D’Aloisio et al. 2020](#)). However, one of the main features of our RT code is that any sub-grid model of IGM opacity can be straightforwardly implemented. We exploit this feature to compare the reionization morphologies in our detailed fiducial simulations against sink models constructed to mimic the various assumptions made previously in the literature.

Another goal of this work is to explore the relationship between reionization sources and sinks. The large uncertainty in the nature of the LyC sources necessitates exploring the sinks in different source models. Although it is widely believed that galaxies were the main drivers of reionization, it remains unclear which galaxies sourced the LyC background (see for example [Robertson et al. 2015](#); [Finkelstein et al. 2019](#); [Naidu et al. 2020](#); [Lewis et al. 2020](#)). A number of studies have looked at the impact of different models for the sources and sinks separately; to our knowledge none have directly addressed the interplay between the two.

This work is organized as follows. In §2, we describe our numerical methods. In §3 we study the morphology of reionization in different sinks models. In §4, we extend our analysis to include different models for the sources. We summarize our results and conclude in §5. Throughout this work, we assume the following cosmological

parameters: $\Omega_m = 0.305$, $\Omega_\Lambda = 1 - \Omega_m$, $\Omega_b = 0.048$, $h = 0.68$, $n_s = 0.9667$ and $\sigma_8 = 0.82$, consistent with the [Planck Collaboration et al. \(2020\)](#) results. All distances are quoted in comoving units unless otherwise specified.

2 NUMERICAL METHODS

2.1 Large-Scale Radiative Transfer

We ran our reionization simulations using the new RT code of [Cain et al. \(2021\)](#). Here we describe the features of the code relevant for this work, leaving a more detailed presentation to a future paper.

The code inputs are a time-series of halo catalogs and coarse-grained density fields from a cosmological N-body simulation. Halos are assigned ionizing photon emissivities and binned to their nearest grid points on the RT grid. Rays are cast from the centers of source cells at each time step. As rays travel, the optical depth through each cell is computed and photons are deposited accordingly. Rays are deleted when they contain $< 10^{-10} \times$ the average number of photons per ray. We use the full speed of light to maintain accuracy at the end of reionization.

As the rays propagate, they adaptively split to maintain a minimum angular resolution around the source cell. When rays from many sources intersect the same cell, the ones with the fewest photons are merged to a fixed level of angular resolution. Splitting and merging is handled with the HealPix formalism ([Gorski et al. 1999](#)) following a procedure similar to the one described in [Abel & Wandelt \(2002\)](#) and implemented in [Trac & Cen \(2007\)](#). The parameters for this are adjustable, allowing the user to trade accuracy for computational time. In Appendix A, we describe these parameters and show that our choices for them are converged in terms of morphology.

To maximize flexibility, our RT algorithm does not explicitly solve for the ionization state of each cell to determine its absorption coefficient, $\bar{\kappa}$. Instead, $\bar{\kappa}$ can be an arbitrary function of density, photo-ionization rate, ionization redshift, and time. Moreover, since our RT cells are large enough to require many RT steps to ionize ($1 h^{-1} \text{Mpc}$ in this work), we track the I-fronts within cells using a “moving screen” approximation. That is, I-fronts are infinitely sharp and the gas behind them is highly ionized. The photo-ionization rate in ionized gas is given by

$$\Gamma_{\text{HI}}^i = \sum_{j=1}^{N_{\text{rays}}} \frac{N_{\gamma,0}^{ij} \bar{\sigma}_{\text{HI}} \bar{\lambda}^i [1 - \exp(-x_{\text{ion}}^i \Delta s_{ij}^{ij} / \bar{\lambda}^i)]}{x_{\text{ion}}^i V_{\text{cell}}^i \Delta t}, \quad (1)$$

where the number of photons in ray j traveling a distance Δs_{ij} through cell i is $N_{\gamma,0}^{ij}$, $\bar{\lambda}^i \equiv 1/\bar{\kappa}^i$ is the mean free path, x_{ion}^i is the ionized fraction, V_{cell}^i is the cell volume, and the sum is over all rays crossing cell i during the time step Δt . The cross-section $\bar{\sigma}_{\text{HI}}$ is averaged over the assumed spectrum of $J_\nu \propto \nu^{-1.5}$ from 1 – 4 Ryd (as in [D’Aloisio et al. 2020](#), motivated by the scaling anticipated in stellar population synthesis models). In partially ionized cells, I-fronts move at a speed $v_{\text{IF}} = F_\gamma / [(1 + \chi) n_{\text{H}}]$, where $\chi = 0.082$ accounts for HeI and F_γ is the leftover photon flux after attenuation by the ionized part of the cell. In Appendix B we show explicitly that Eq. 1 is valid for arbitrary $\bar{\kappa}$.

2.2 Sub-grid model for $\bar{\lambda}$

In standard RT, Eq. 1 would be closed by an ionization balance equation (perhaps including a sub-grid clumping factor) and $\bar{\lambda}$ computed

from the HI fraction. Our fiducial setup instead uses a prescription for $\bar{\lambda}$ based on an extended suite of the small-volume hydro plus ray-tracing RT simulations first presented in D’Aloisio et al. (2020). These were run with a modified version of the RadHydro code (Trac & Pen 2004; Trac & Cen 2007) in 1 (Mpc/h)^3 volumes with $N = 1024^3$ DM particles, gas and RT cells. We ionize the whole volume at $z = z_{\text{reion}}$ by sending I-fronts from the boundaries of $L_{\text{dom}} = 32 h^{-1} \text{kpc}$ domains. This setup avoids complicating the interpretation of our results with uncertain galaxy physics by treating the gas as if it were reionized by external sources. The photo-ionization rate $\Gamma_{-12} \equiv \Gamma_{\text{HI}}/(10^{-12} \text{ s}^{-1})$ is constant in optically thin gas. (We emphasize, however, that our simulations explicitly include self-shielding systems and associated RT effects.) We simulated over-dense and under-dense regions by using the method of Gnedin et al. (2011) to account for box-scale density fluctuations. These are parameterized by δ/σ , the linearly extrapolated over-density in units of its standard deviation. We refer the reader to D’Aloisio et al. (2020) for more details¹.

We estimate $\bar{\lambda}$ in our RadHydro simulations using

$$\bar{\lambda}^{-1} \equiv \bar{\kappa} = \frac{\langle \Gamma_{\text{HI}} n_{\text{HI}} \rangle_V}{F_\gamma}, \quad (2)$$

where F_γ is the ionizing photon flux in each domain. In Appendix C we show that the right-hand side of Eq. 2 is equal to the volume-averaged absorption coefficient and is the relevant quantity for evaluating Eq. 1. Note that this definition of $\bar{\lambda}$ accounts for non-equilibrium absorptions by self-shielded systems (e.g. mini-halos), an effect that cannot be accurately captured with a clumping factor (as noted by McQuinn et al. 2007; Shukla et al. 2016).

Our RadHydro simulations give us $\bar{\lambda}$ versus time in a range of environments parameterized by $(z_{\text{reion}}, \Gamma_{\text{HI}}, \delta/\sigma)$. While we could simply interpolate over these parameters to get $\bar{\lambda}^i$ in Eq. 1, doing so would neglect the sensitivity of $\bar{\lambda}$ to the time-evolution of Γ_{HI} , since Γ_{HI} does not evolve in the small-volume simulations. This sensitivity arises from the dependence of the relaxation process on the self-shielding properties of the gas, which are set by largely by Γ_{HI} (see Figs. 5 and 6 of D’Aloisio et al. 2020). We incorporated this Γ_{HI} -dependence using an empirically-motivated model for the full time-evolution of $\bar{\lambda}$,

$$\frac{d\bar{\lambda}}{dt} = \frac{\partial \bar{\lambda}}{\partial t} \Big|_{\Gamma_{\text{HI}}} + \frac{\partial \bar{\lambda}}{\partial \Gamma_{\text{HI}}} \Big|_t \frac{d\Gamma_{\text{HI}}}{dt} - \frac{\bar{\lambda} - \bar{\lambda}_0}{t_{\text{relax}}}, \quad (3)$$

where the first term captures the time-dependence of $\bar{\lambda}$ at fixed Γ_{HI} , and the second the instantaneous change in $\bar{\lambda}$ with Γ_{HI} . The former is interpolated from our small-volume simulation suite, and for the latter we assume a power law $\bar{\lambda} \propto \Gamma_{\text{HI}}^{2/3}$, consistent with the scaling found in simulations (e.g. McQuinn et al. 2011). The last term captures the evolution of $\bar{\lambda}$ towards the constant- Γ_{HI} limit $\bar{\lambda}_0$ (also interpolated from our small-volume suite). Here t_{relax} is the timescale over which the gas loses memory of its previous Γ_{HI} history, which we take to be 100 Myr. In Appendix D, we show that Eq. 3 compares well against small-volume simulations with evolving Γ_{HI} . Since $\bar{\lambda}$ is a function of Γ_{HI} , Eqs. 1 and 3 are iterated five times for each time step, which we find sufficient for convergence (Appendix A).

¹ Our expansion of the suite in D’Aloisio et al. (2020) includes all combinations of $z_{\text{reion}} \in \{6, 8, 12\}$, $\Gamma_{-12} \in \{0.03, 0.3, 3.0\}$ and $\delta/\sigma \in \{-\sqrt{3}, 0, \sqrt{3}\}$. Due to computational limitations, not all of our small-volume simulations are run to when reionization ends ($5 < z < 6$). In these cases we extrapolate the results to lower redshifts by fitting $\bar{\lambda}$ to a power law in cosmic time over the last 50 Myr of the run.

2.3 Caveats

Here we will briefly discuss two caveats to our sub-grid model. The first is that our small-volume simulations should under-produce massive halos, which can act as sinks. This may be true even in our over-dense DC mode runs, which sample biased regions of the IGM where these halos are more common. This would be most problematic at the lowest redshifts when rare, massive sinks contribute significantly to the IGM opacity (Nasir et al. 2021)².

The second, concerns our treatment of self-shielded gas. Eq. 2 for $\bar{\lambda}$ accounts for absorptions by self-shielded gas clumps that remain neutral some time after I-front passage (Nasir et al. 2021). The gas in these systems can be a significant fraction of the gas in the cell within 50 Myr of ionization when Γ_{HI} is low ($\lesssim 10^{-13} \text{ s}^{-1}$). In principle, this gas should be excised from our moving-screen I-front calculation, which counts 1 absorption per neutral atom during I-front passage. As such, gas that remains neutral for more than a few Myr after I-front passage is effectively treated as if it were ionized twice. We have run a conservative test in which we derive $\bar{\lambda}$ in the small-volume simulations using the recombination clumping factor C_R (Eq. 5 of D’Aloisio et al. 2020) under the assumption of photo-ionizational equilibrium. This approach ignores the fact that some of the neutral gas is ionized after I-front passage and counts only recombination-balanced absorptions (see §3.2 in the next section for more details). Thus using C_R likely under-estimates the photon budget and brackets the magnitude of the double-counting effect. We found that the difference between the number of absorptions in ionized gas between using C_R and our fiducial model can be as high as a factor of 2 when low- Γ_{HI} gas dominates the absorption rate. Thus the photon budget predicted by our fiducial sinks model is almost certainly too high, although which model is closer to the truth is unclear. Fortunately, the impact on our results is minimal because, as we will see, the sinks probably do not shape morphology substantially under most circumstances. Even so, our results using this model should be interpreted as an upper limit on the expected effect of un-relaxed gas. In what follows we will make note whenever this point becomes relevant.

2.4 Density Fields & Sources

The density and source fields for our large-volume RT simulations are taken from a cosmological N-body DM-only simulation in a $300 h^{-1} \text{Mpc}$ box run using MP-Gadget (Feng et al. 2018). The run used $N = 2048^3$ DM particles, for a mass resolution of $2.5 \times 10^8 h^{-1} \text{M}_\odot$ and a minimum halo mass of $8.5 \times 10^9 h^{-1} \text{M}_\odot$ (corresponding to 32 DM particles). The DM particles were smoothed onto a grid with $1 h^{-1} \text{Mpc}$ cells to get the density fields for the RT calculation. Density and halo fields are updated every 10 Myr from $z = 12$ to 4.5, for a total of 99 snapshots. The RT time-step is equal to the light-crossing time of the RT cells, and varies from ≈ 0.4 to ≈ 0.8 Myr during the simulation. When the density field is updated, we keep the same ionized fractions in all cells - thus we neglect the advection of ionized/neutral gas between snapshots. This should be a reasonable approximation since bulk velocities on $\gtrsim 1 h^{-1} \text{Mpc}$ scales are typically slower than the speed of ionization fronts (a few hundred vs. $10^3 - 10^4 \text{ km/s}$). We populated halos with galaxies by abundance matching to the UV luminosity function of Finkelstein et al. (2019).

² In Cain et al. (2021), this issue partially motivated the enhanced sinks model, which appealed to missing rare sinks to help explain the mild evolution of the mean free path at $z < 5$.

Halos with masses well below $8.5 \times 10^9 h^{-1} M_\odot$ likely formed stars via atomic cooling, and so may have contributed significantly to reionization. We thus extended the halo mass function (HMF) of our simulation using a modified version of the non-linear biasing method of Ahn et al. (2015). These “sub-resolved” halos follow the HMF of Watson et al. (2013) (which agrees with our resolved HMF) and are spatially distributed following the extended Press-Schechter (EPS) formalism. The number of added halos in each cell and mass bin is drawn randomly from a Poisson distribution with mean equal to the halo abundance predicted by EPS. We found that the clustering of the halos predicted by this formalism was systematically higher than that in the SCORCH simulations (Trac et al. 2015). Specifically, the halo bias produced by the EPS method was a factor of 1.4 (1.32, 1.18) too high compared to SCORCH at $z = 10$ (8, 6). We therefore added an empirically derived bias correction to the model to approximately reproduce the clustering of SCORCH halos in the mass range of interest.

We extended the HMF in our simulations to a minimum mass of $M_{\min} = 10^9 h^{-1} M_\odot$. Emissivities were assigned to halos assuming that the emissivity of each halo follows a power law in UV luminosity, $\dot{n}_\gamma \propto L_{\text{UV}}^\beta$. Smaller M_{\min} and β correspond to reionization driven by fainter, less biased sources. Our fiducial model has $M_{\min} = 10^9 h^{-1} M_\odot$ and $\beta = 1$, which corresponds to assuming a single value of the escape fraction f_{esc} and ionizing efficiency ξ_{ion} for the entire source population at each redshift. We chose this as our fiducial model for two reasons: (1) it imposes minimal assumptions about the dependence of f_{esc} and ξ_{ion} on halo mass and (2) of the models we will consider, it is the most similar to models commonly used in reionization simulations (e.g. $n_\gamma \propto M$ as in Keating et al. (2020a) and Mao et al. (2020)). In §4 we study what happens when M_{\min} and β are varied. In all simulations, the global emissivity is specified as a user-input to produce a reionization history similar to the fiducial late-ending rapid model of Cain et al. (2021).

3 THE EFFECT OF SINKS ON REIONIZATION’S MORPHOLOGY

3.1 Sinks Models

In this section, we discuss the effect of sinks on the morphology of reionization. We compare our new sinks model to several representative alternatives. We assume our fiducial source model throughout (in §4 we will explore others.) We compare the following sink prescriptions:

- **Full Sinks:** Our fiducial sinks model is based on the suite of RadHydro simulations as described in § 2.2. The evolution of $\bar{\lambda}$ in each cell includes the dynamical effects of pressure smoothing and photoevaporation, as well as the impact of sub-resolved self-shielding on the IGM opacity.

- **Relaxed Limit:** For this model, we extrapolate the low-redshift $\bar{\lambda}$ from our $z_{\text{reion}} = 12$ RadHydro simulations to higher redshifts, assuming a power law in cosmic time, and directly interpolate $\bar{\lambda}$ instead of using Eq. 3. Thus, the gas is treated in the limit that it was ionized long ago and has reached a pressure-smoothed equilibrium. This model effectively removes the contribution of opacity from the initial clumpiness that is eventually erased during the relaxation process.

- **Sub-grid Clumping Factor:** Here we assume that all gas in ionized regions is in photo-ionization equilibrium, which yields

$$\bar{\lambda} = \frac{\Gamma_{\text{HI}}}{\sigma_{\text{HI}} C_{\text{HII}} \alpha_B(T)(1+\chi)n_{\text{H}}^2}, \quad (4)$$

where α_B is the case B recombination coefficient of ionized hydrogen, $C_{\text{HII}} \equiv \langle n_{\text{HII}}^2 \rangle / \langle n_{\text{HII}} \rangle^2$ is the *sub-grid* ionized hydrogen clumping factor (note this is different from C_R mentioned in §2.3 in that it does not include temperature fluctuations through α_B). We adopt two prescriptions for C_{HII} :

- (i) **Uniform C_{HII} :** We set $C_{\text{HII}} = 6$ everywhere at all times, which reproduces a reionization history and photon budget similar to the Full Sinks model. This case serves as a basis for comparison to assess the importance of the dynamics and spatial in-homogeneity of the sinks predicted by the Full Sinks model. We emphasize that C_{HII} is a sub-grid clumping factor, not a global one.

- (ii) **Maximum $C_{\text{HII}}(\Delta)$:** We use the density-dependent sub-grid clumping factor of Mao et al. (2020).³ This model is based on dark-matter-only N-body simulations and predicts $C_{\text{HII}} \approx 10 - 15$ in cells with $\Delta \geq 1$ at $z \leq 8$. Since this model neglects pressure smoothing effects, it represents an upper limit on the amount of clumping in the standard cosmology.

The left-most panel in Figure 1 shows the volume-averaged ionized fraction for each sinks model alongside measurements from the literature. The middle panel shows the global ionizing emissivity. The emissivity histories are all re-scaled versions of the “rapid” model from Cain et al. (2021). For comparison, the emissivities of the Full Sinks, Relaxed Limit, and Uniform C_{HII} models have been tuned to yield very similar reionization histories and ionizing photon budgets, ending reionization late at $z = 5 - 5.5$. The Maximum $C_{\text{HII}}(\Delta)$ emissivity was tuned to end reionization somewhat earlier because the clumping factor fits from Mao et al. (2020) do not extend below $z \sim 6.5$.⁴ However, the ensuing morphology comparisons will be performed at fixed global ionized fraction, which should minimize any differences originating from the different reionization histories. Note that the Full Sinks and Uniform C_{HII} models have the same emissivity, while the Relaxed Limit (Maximum $C_{\text{HII}}(\Delta)$) emissivity is a factor of 0.7 (2.4) smaller (larger) than the other two. We note that due to the over-counting issue discussed in §2.3, the emissivity in the Full Sinks and Uniform C_{HII} models are likely higher than they should be. A lower photon budget would mean a smaller C_{HII} in the latter to match the Full Sinks case; thus the value of $C_{\text{HII}} = 6$ is probably too high. In the ensuing discussion we will see that our main conclusions on morphology are not significantly affected by this issue.

The right-most panel of Figure 1 shows Γ_{HI} averaged over fully ionized cells for each model, compared to measurements from Becker & Bolton (2013). Here we omit $z > 5$ measurements (e.g. Calverley et al. 2011; Wyithe & Bolton 2011; D’Aloisio et al. 2018; Becker et al. 2021) for clarity, and also because it is unclear how to compare these measurements against our Γ_{HI} in simulations where reionization is still ongoing at $z = 5 - 6$. A number of reionization observables are

³ Note that the large-volume simulations in Mao et al. (2020) have smaller cells than ours, so their clumping factors are a slight under-estimate for our application. Still, this model serves the purpose of illustrating how the morphology evolves in an extremely clumpy IGM, which is our goal.

⁴ We extrapolate the Mao et al. (2020) fitting parameters to slightly lower redshifts by assuming their a_0 parameter evolves linearly in redshift, while a_1 and a_2 retain their $z = 6.5$ values (see their Eq. 17 and appendix B.)

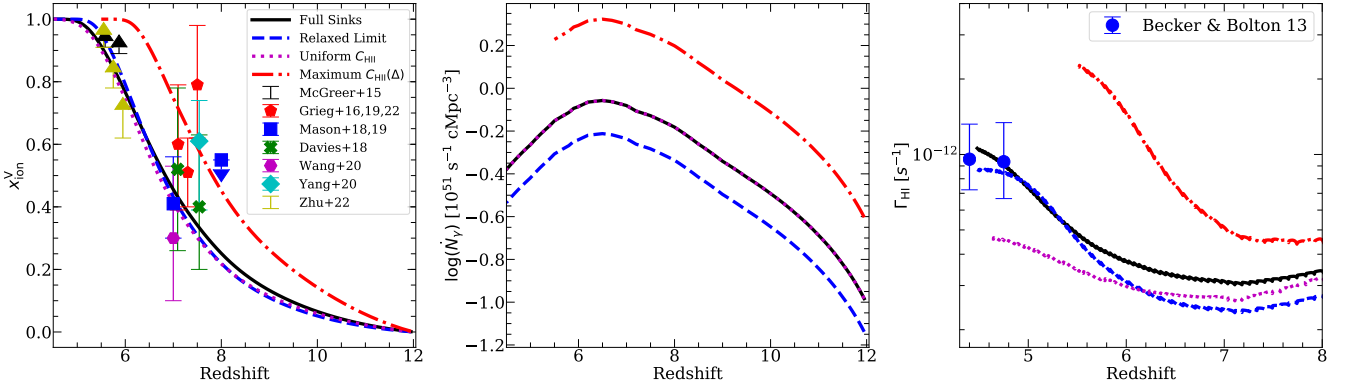


Figure 1. Volume-averaged ionized fraction (left), co-moving total ionizing emissivity (middle), and average photo-ionization rate in fully ionized cells (right) for each sinks model. All results shown here adopt our fiducial source scenario. We include measurements from the literature in the left panel (McGreer et al. 2015; Greig et al. 2016; Greig et al. 2019; Davies et al. 2018; Mason et al. 2018; Wang et al. 2020; Yang et al. 2020; Greig et al. 2022; Zhu et al. 2022). All the reionization histories are similar except the Maximum $C_{\text{HII}}(\Delta)$ case. In the ensuing discussion, we show that the Full Sinks and Uniform C_{HII} models have nearly indistinguishable morphologies assuming our fiducial source model. Notably, although these models have the same reionization and emissivity histories, they have significantly different photo-ionization rates. Hence they may be distinguishable by observables that are sensitive to Γ_{HI} , e.g. the mean free path and the Ly α forest.

explicitly sensitive to Γ_{HI} , including the mean free path, Ly α forest statistics, and LAE visibility. In the ensuing discussion we will show that the Full Sinks and Uniform C_{HII} models exhibit essentially identical morphologies in our fiducial source model. A key takeaway from Figure 1 is that sink models tuned to yield similar morphologies, e.g. the Full Sinks and Uniform C_{HII} models, may nonetheless exhibit considerable differences in observables that are sensitive to Γ_{HI} . So while these models may appear nearly identical in their predictions for the 21cm power spectrum, they will yield different predictions for e.g. Ly α forest statistics.

3.2 Visualization of the IGM Opacity

To aid in visualizing the dynamics and spatial morphology of the sinks, we define the “effective clumping factor” for cell i to be

$$C_{\text{eff}}^i = \frac{(1/\bar{\lambda}^i)}{\sigma_{\text{HI}} \alpha_B(T_{\text{ref}})(1+\chi)n_{\text{H}}^{i,2}/\Gamma_{\text{HI}}^i}, \quad (5)$$

where $T_{\text{ref}} = 10^4$ K and Γ_{HI}^i , $\bar{\lambda}^i$, and $n_{\text{H}}^{i,2}$ are the photo-ionization rate, mean free path, and H number density, respectively. The numerator is simply the absorption coefficient κ , and the denominator is what κ would be if the gas had a constant temperature T_{ref} , was in photo-ionizational equilibrium, and had no sub-resolved density fluctuations. C_{eff} quantifies the impact of sub-grid sink physics and large-scale temperature fluctuations on the opacity. In the limit of photo-ionizational equilibrium, Eq. 5 is equivalent to the recombination clumping factor C_R (see § 2.3). Differences between C_{eff} and C_R indicate the presence of sub-resolved self-shielded systems that are not in photo-ionizational equilibrium. Note that unlike in D’Aloisio et al. (2020), the density in the denominator of our clumping factors is the *cell-wise* density rather than the cosmic mean density. Thus, density fluctuations influence C_{eff} only indirectly through their impact on the sub-resolved clumpiness of the gas and its self-shielding properties.

For intuition on C_{eff} , Figure 2 shows its evolution (dashed curves) compared to that of C_R (dotted curves) vs. time since ionization for two of our mean density, $z_{\text{reion}} = 8$ small-volume RadHydro simulations. One has $\Gamma_{-12} = 3.0$ (black), and the other 0.03 (blue). In the first case, C_{eff} and C_R are close together; both start above

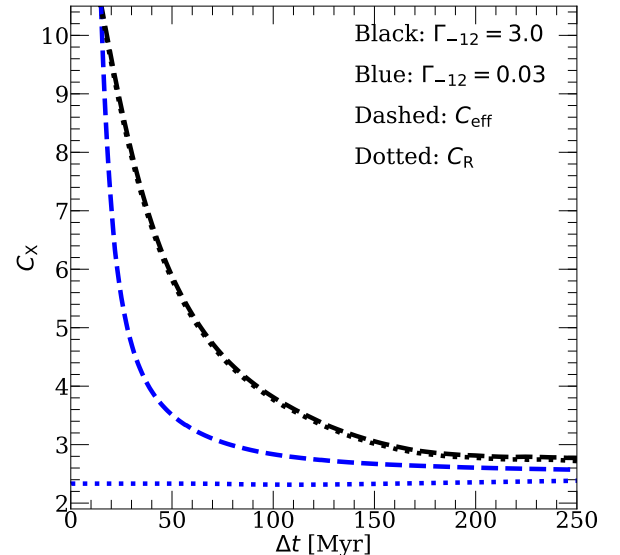


Figure 2. Examples of C_{eff} (dashed) compared to C_R (dotted) for small-volume simulations with high and low values of Γ_{-12} (3.0 and 0.03). In the former, the two quantities are similar owing to the scarcity of self-shielded gas. However for $\Gamma_{-12} = 0.03$, systems remain self-shielded and out of equilibrium for longer, producing a large difference between C_{eff} and C_R since the former reflects the total number of absorptions but the latter only those balanced by recombinations.

10 and approach ~ 3 as the gas relaxes. Their similarity owes to the high intensity of the background, which leaves little gas self-shielded. In the $\Gamma_{-12} = 0.03$ case, there is significant self-shielding in high-density gas. This lowers C_R (which counts only recombination-balanced absorptions), while C_{eff} remains elevated, since it is affected by non-equilibrium absorptions taking place as the self-shielded gas is ionized. At later times, C_{eff} and C_R agree better as more self-shielded systems evaporate.

Figure 3 shows slices of $\log(C_{\text{eff}})$ from large-volume simulations for each of our sinks models (assuming our fiducial source model). We show the Full Sinks (left-most), Relaxed Limit (middle-left), Uniform C_{HII} (middle-right) and Maximum $C_{\text{HII}}(\Delta)$ (right).

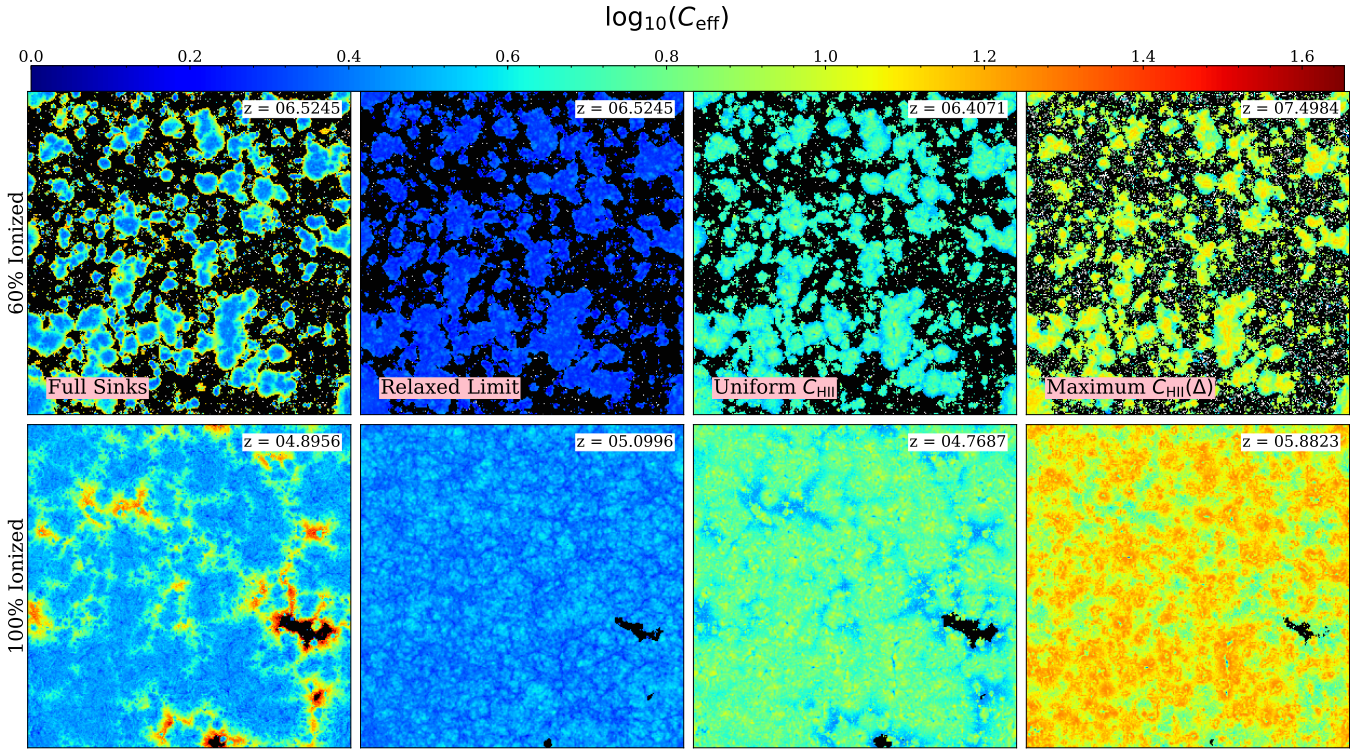


Figure 3. Visualization of the sink physics in each of our models. The redshifts are noted in the upper right of each panel. We show $\log_{10}(C_{\text{eff}})$ at 60% volume ionized fraction (top) and 50 Myr after reionization ends ($x_{\text{ion}}^V < 0.01$, bottom row). The black regions denote cells that are at least 50% (10%) neutral in the top (bottom) panels. In the Full Sinks case, the opacity is boosted near I-fronts (top) and in under-dense voids that have yet to relax after reionization ends (bottom). The large scale fluctuations in C_{eff} are weaker in the other models. In the Uniform C_{eff} and Maximum $C_{\text{HII}}(\Delta)$ models, C_{eff} is lower than average in voids after reionization, in contrast to the Full Sinks case. These visualizations illustrate the dynamical effects of pressure smoothing and photoevaporation in our Full Sinks model.

most) models at 60% volume ionized in the top row, and 50 Myr after reionization has finished ($x_{\text{ion}}^V = 0.01$) in the bottom row. The redshifts are given in the upper right of each panel. In the top (bottom) row, black regions denote cells that are at least 50% (10%) neutral (note that a small number of cells are still partially neutral even after $x_{\text{ion}}^V < 0.01$ in the bottom row). In the Full Sinks model, C_{eff} is highest near I-fronts where gas was most recently ionized. After reionization ends, patches of enhanced opacity with $C_{\text{eff}} \sim 10 - 20$ (and even higher in the most recently ionized cells) persist in the voids, which ionized last and quickly, so have yet to relax. In regions re-ionized earlier, C_{eff} is $\sim 2 - 5$ at all redshifts, similar to the Relaxed Limit. The opacity is higher in the Uniform C_{HII} case than in the Relaxed Limit because it has been calibrated to match the photon budget of the Full Sinks model. The Maximum $C_{\text{HII}}(\Delta)$ model has the highest opacity, with $C_{\text{eff}} \sim 10 - 20$ everywhere after reionization.

A comparison between the top-left and the two top-right panels in Fig. 3 reveals that the opacity in over-dense regions hosting the earliest ionized bubbles is significantly lower in our Full Sinks model compared to the Uniform C_{HII} and Maximum $C_{\text{HII}}(\Delta)$ models. This results from the dynamics in our Full Sinks model, and may arise from two effects working in tandem: (1) Γ_{HI} is generally larger near the highly clustered sources, which leads to a quicker relaxation/evaporation of the sinks nearby ; (2) The structures that form in these regions may have a shorter relaxation time owing to their larger densities (see e.g. Eq. 4 of D’Aloisio et al. 2020). Together, these effects in our Full Sinks model work towards favoring the growth of larger bubbles compared to the Uniform C_{HII} and

Maximum $C_{\text{HII}}(\Delta)$ models. Conversely, the opacity is elevated in recently ionized regions at lower redshifts, near the end of reionization, despite being under-dense on average. Hence the topology of C_{eff} in the Full Sinks model is inverted with respect to the other three models, i.e. C_{eff} is larger in the under-dense voids that reionize last.

In the other three models, C_{eff} is affected mainly by temperature and density fluctuations. The imprint of temperature fluctuations is most noticeable in the Uniform C_{HII} and Maximum $C_{\text{HII}}(\Delta)$ models, producing lower C_{eff} in voids that were heated most recently by reionization. In the Maximum $C_{\text{HII}}(\Delta)$ model this trend is further enhanced by the strong density dependence of C_{HII} . We emphasize that the contrasting C_{eff} topologies will affect any observables that are explicitly sensitive to Γ_{HI} and the opacity structure of the IGM, such as the Ly α forest and the mean free path (see discussion of Fig. 1). However, in the ensuing discussion we will see that they are probably not very important for morphology.

3.3 Ionized Bubbles

3.3.1 Visualization of Ionized Region Morphology

Figure 4 shows the ionization field (darker = more neutral) for each of our sinks models (top to bottom, see labels) at 20, 50, and 80% volume ionized fraction (left to right). At fixed ionized fraction, the Maximum $C_{\text{HII}}(\Delta)$ model exhibits the smallest ionized bubbles. All the other models are visually similar except at 20% ionized, when the Relaxed Limit has slightly larger bubbles than the other two. The largest bubbles are smaller in the Maximum $C_{\text{HII}}(\Delta)$ model because the sources driving their growth are “taxed” disproportionately by

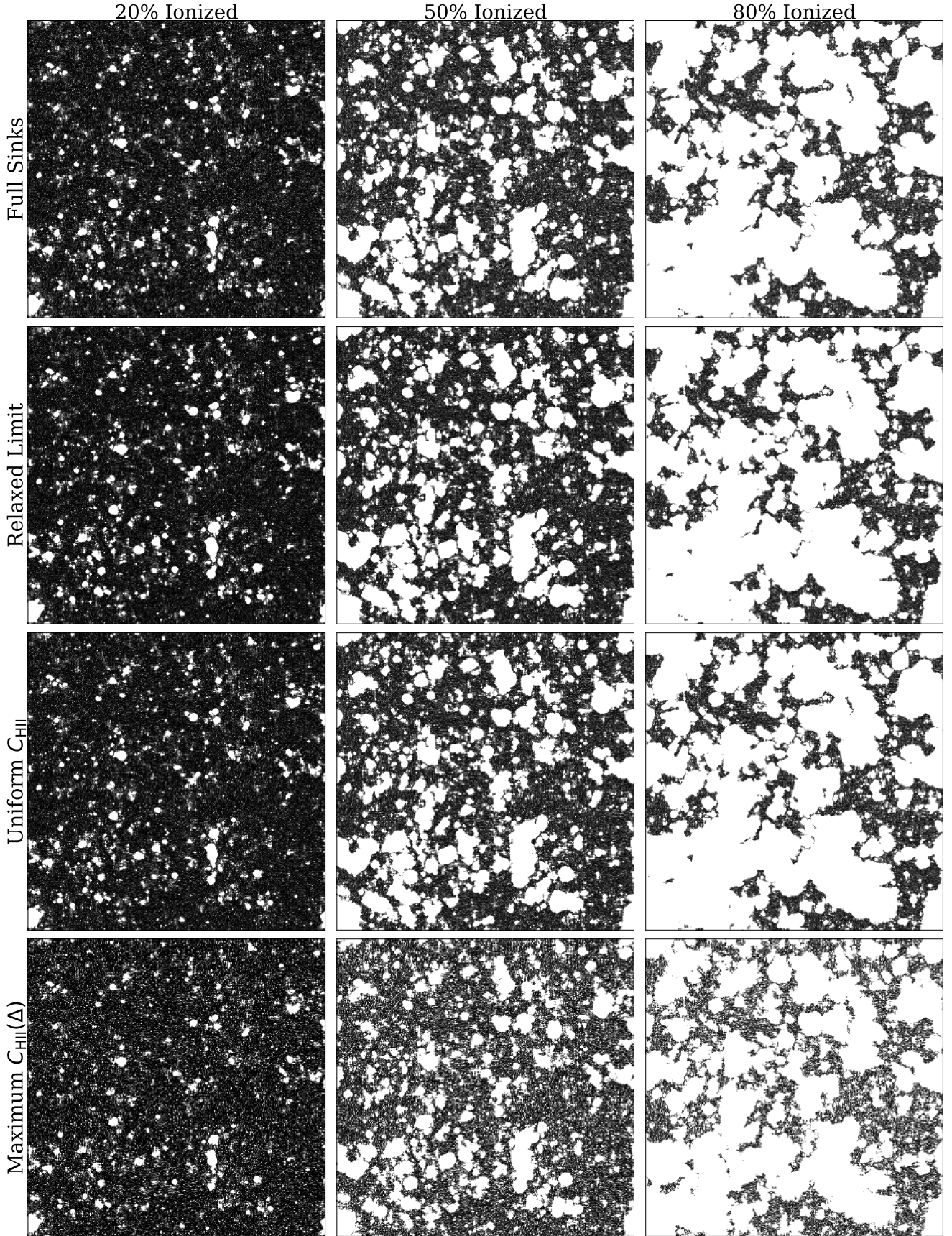


Figure 4. Visualization of the ionization field for our sinks models. All results here correspond to our fiducial source model with $\dot{n}_\gamma \propto L_{\text{UV}}$, i.e. assuming the same escape fraction and ionizing efficiency for all sources. The columns show different volume ionized fractions (20, 50, and 80%, left to right) and the rows show different sinks models. The ionized bubbles are smallest in the Maximum $C_{\text{HII}}(\Delta)$ model at all ionized fractions. The Relaxed Limit model has slightly larger bubbles at 20% ionized than the Full Sinks and Uniform C_{HII} models, but these three models are otherwise visually similar.

recombinations compared to those in smaller bubbles (Furlanetto & Oh 2005).⁵ Since large bubbles form in over-densities and start growing the earliest, their growth is slowed by recombinations sooner than their later-forming counterparts inhabiting lower densities. Thus the sinks act to reduce the average bubble size at fixed ionized fraction (as found by e.g. Furlanetto & Oh 2005; McQuinn et al. 2007; Alvarez & Abel 2012; Mao et al. 2020; Chen et al. 2022).

Comparing the Full Sinks (top row) and Maximum $C_{\text{HII}}(\Delta)$ (bottom row) models, the ionized bubbles generally appear larger in the former at fixed ionized fraction. As described in the previous section, this is a direct result of the dynamics in our sub-grid sinks model. In the earliest bubbles to form around highly clustered sources, the sinks relax/evaporate quickly, allowing the bubbles to grow more easily. By contrast, the smaller bubbles that start growing around less biased sources generally encounter a clumpier IGM for longer periods of time. Together, these effects work toward favoring the growth of large bubbles and partially cancel the “taxing the rich” effect described in the previous paragraph. The Maximum C_{HII} model instead has higher clumping factors at higher densities, which slows the growth of the largest bubbles more. In other words, our Full Sinks model taxes the rich *less* than the Maximum $C_{\text{HII}}(\Delta)$ model, which does not include any dynamical effects.

Interestingly, in Figure 4 we see a striking degree of similarity between the Full Sinks and Uniform C_{HII} models at all ionized fractions. In fact, these models do not even differ significantly from the Relaxed Limit except near the beginning of reionization. The visual similarity leads us to one of our key conclusions, which we will hash out quantitatively in the ensuing sections. Accounting for the pressure-smoothing of the IGM by reionization is crucial for modeling morphology accurately. However, as long as this effect is accounted for “on average,” e.g. in the simplest case with a uniform sub-grid clumping factor, the detailed dynamics and spatial in-homogeneity of the sinks are likely not very important for morphology. We emphasize, however, that this conclusion holds only for source models in which bright galaxies contribute significantly to the ionizing photon budget, as in our fiducial source model. In §4, we will see scenarios for which the details of the sink modeling *do* become quite important.

3.3.2 Bubble Size Distribution

Next we study morphology more quantitatively using the ionized bubble size distribution (IBSD). We compute the IBSD using the ray-tracing definition proposed in Mesinger & Furlanetto (2007) and implemented in the publicly available package *tools21cm* (Giri et al. 2018). The IBSD defined this way captures the distribution of distances to neutral gas along random rays starting in ionized regions, and thus quantifies bubble sizes well even after ionized regions overlap.

Figure 5 (top row) shows the IBSD at 20%, 50%, and 80% (left to right) for our sinks models. The IBSD confirms that the Maximum $C_{\text{HII}}(\Delta)$ has the smallest bubbles at all times, and that the other three models have similar bubble sizes. The average bubble size is given at 20%, 50%, and 80% ionized for each model in Table 1. The bubble sizes for the Full Sinks and Uniform C_{HII} models are nearly identical at all ionized fractions. At 20% and 50% ionized the Relaxed Limit model has slightly larger bubbles, but at 80% ionized is indistinguishable from the Full Sinks and Uniform C_{HII} models. We see from the Relaxed Limit comparison that even

⁵ This has been termed “taxing the rich” by Furlanetto & Oh (2005).

Mean Bubble Size [$h^{-1}\text{Mpc}$]	20%	50%	80%
Full Sinks	1.91	7.53	32.09
Relaxed Limit	2.45	8.47	31.30
Uniform C_{HII}	1.89	7.56	31.92
Maximum $C_{\text{HII}}(\Delta)$	1.11	4.58	22.39

Table 1. Mean ionized bubble size at 20%, 50%, and 80% ionized for each of the sinks models in this section.

assuming a fully pressure-smoothed IGM at all times is a reasonable approximation for morphology, especially late in reionization.

3.4 21 cm Power Spectrum

The 21 cm power spectrum, which probes the H I fluctuations in the IGM, is being targeted by PAPER (Parsons et al. 2010), MWA (Tingay et al. 2013), LOFAR (Yatawatta et al. 2013), HERA (DeBoer et al. 2017; Abdurashidova et al. 2022b,a), and forthcoming experiments such as SKA (Koopmans et al. 2015). Ignoring redshift-space distortions and assuming the spin temperature of the 21 cm transition T_S is much greater than the CMB temperature, we can write the 21 cm brightness temperature at position \vec{x} as

$$T_{21}(\vec{x}) = \overline{T_{21}}x_{\text{HI}}(\vec{x})(1 + \delta(\vec{x})) \quad (6)$$

where $\overline{T_{21}}$ is T_{21} at mean density in neutral gas, which depends on redshift and cosmology only⁶, x_{HI} is the H I fraction, and $1 + \delta$ is the gas density. The dimensionless 21 cm power spectrum is $\Delta_{21} \equiv k^3/2\pi^2 P_{21}(k)$, where $P_{21}(k)$ is the power spectrum of T_{21} . Since Δ_{21} depends on x_{HI} , it is sensitive to the differences in morphology between our sinks models.

Figure 5 (bottom row) shows Δ_{21} vs. wavenumber k for our sinks models at 20%, 50%, and 80% ionized fractions (left to right). In all cases we see familiar qualitative features. Early on, Δ_{21} is steep in k and its amplitude on large scales reaches a local minimum – a result of inside-out reionization (McQuinn & D’Aloisio 2018; Giri et al. 2019b). Later, Δ_{21} flattens out and its amplitude at $k \leq 0.2 h^{-1}\text{Mpc}$ has increased by 1–2 orders of magnitude by an ionized fraction of 80%. (Note the different y axes on different panels.) This happens because the ionization field, which fluctuates on scales characteristic of the largest ionized bubbles (10 – $30 h^{-1}\text{Mpc}$), takes over for the density field as the main driver of Δ_{21} at small k .

The main effect of sinks is to reduce Δ_{21} on large scales ($k \leq 0.5 h\text{Mpc}^{-1}$) by decreasing the sizes of large ionized bubbles. At 20% ionized, Δ_{21} at $k = 0.1 h\text{Mpc}^{-1}$ for the (Relaxed Limit, Maximum $C_{\text{HII}}(\Delta)$) model is (1.75, 0.74) times its Full Sinks model value. At 50% ionized these numbers become (1.16, 0.53), and at 80% ionized, they are (1.0, 0.74). In all panels the Full Sinks and Uniform C_{HII} models are always within a few percent of each other. We see that the Maximum $C_{\text{HII}}(\Delta)$ model, which neglects the effects of pressure smoothing, under-estimates the large-scale Δ_{21} by ≈ 25 – 45% relative to the Full Sinks case during much of reionization. The Relaxed Limit over-estimates the power substantially only at 20% ionized, and becomes an increasingly better approximation as reionization progresses.

The Maximum $C_{\text{HII}}(\Delta)$ model illustrates that neglecting pressure

⁶ Specifically, $\overline{T_{21}}^2 \propto 1+z$. Since our Maximum $C_{\text{HII}}(\Delta)$ model has a somewhat earlier re-ionization history, when comparing to that model we re-scale $\overline{T_{21}}$ to bring it to the same redshift as the other models. Thus our comparisons reflect only differences sourced by x_{HI} .

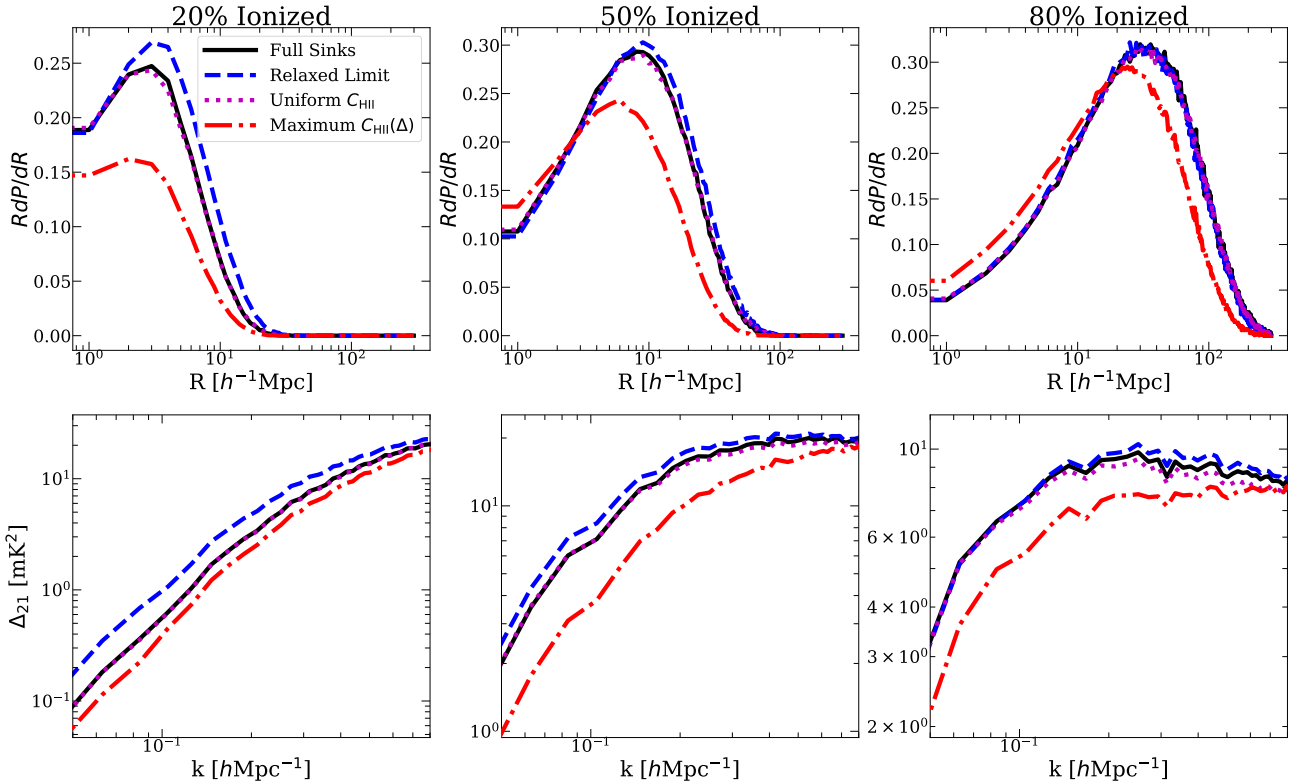


Figure 5. Top: Ionized Bubble Size Distribution (IBSD) for our sinks models (see legend) at 20%, 50%, and 80% volume ionized fractions (left to right). The Full Sinks and Uniform C_{HII} models have strikingly similar IBSDs despite their very different clumping topologies. **Bottom:** 21 cm power (Δ_{21}) vs. wavenumber for the same models and ionized fractions. At 20% ionized, the Maximum $C_{\text{HII}}(\Delta)$ model is well below the Relaxed Limit, with the other two models in between, but closer to the Maximum $C_{\text{HII}}(\Delta)$ result. At later times, the Full Sinks and Uniform C_{HII} models (which are always very similar to each other) move close to the Relaxed Limit. All results shown here adopt our fiducial source model with $\dot{n}_\gamma \propto L_{\text{UV}}$.

smoothing can lead to a significant under-estimate of the large-scale power, owing to that model’s smaller ionized bubbles. On the other hand, assuming a fully relaxed IGM likely over-estimates the power early on, but becomes a reasonable approximation in the last half of reionization. Finally the similarity of the Full Sinks and Uniform C_{HII} models suggests that Δ_{21} is unlikely to be sensitive to the details of how sinks are modeled, as long as the dynamics of the sinks can be accounted for in an average fashion via a uniform sub-grid clumping factor. We caution, however, that all of these conclusions are sensitive to the properties of the sources, and we have employed only our fiducial source model so far. As we will see in §4.2, the impact of sinks becomes larger (smaller) when fainter (brighter) sources dominate the photon budget.

3.5 Neutral Islands

So far our focus has been the morphology of ionized bubbles during the bulk of reionization. However, a lot of progress toward understanding reionization is being made with the growing number of $z > 5$ QSO absorption spectra, which may be probing the final phases of reionization when the mostly ionized IGM was punctuated by islands of neutral gas.⁷ Here we will briefly explore the morphology of these “neutral islands”. Neutral islands have been the focus of a number

of recent studies (e.g. Xu et al. 2014; Malloy & Lidz 2015; Xu et al. 2017; Giri et al. 2019a; Wu et al. 2022) owing to their importance for late-reionization observables.

In Figure 6, we illustrate the distribution of neutral gas at 10% volume neutral fraction using slices through our simulations. The red shading in each panel corresponds to neutral regions that are ionized in the Full Sinks model, i.e. to highlight differences in the neutral island morphology with that model. We see that the neutral islands in the Relaxed Limit and Uniform C_{HII} models differ very little from the Full Sinks case, while there are substantial differences with the Maximum $C_{\text{HII}}(\Delta)$ model. In that model the neutral structures are more extended – as illustrated in red – but also appear to be a lighter shading of gray. This lighter shading indicates that the neutral islands are more porous, i.e. they contain a larger number of small ionized bubbles inside of them.

We quantify the morphology with the neutral island size distribution (NISD), defined analogously to the IBSD. Late in reionization, the NISD is sensitive to the definition of a “neutral” cell, since most of the cells with neutral gas are partially ionized, especially in models with high opacity. We define a cell to be part of an island if $x_{\text{HI}} > 0.01$. This choice is motivated by the fact that a sightline intersecting a partially neutral cell must pass within 1 Mpc/h of an ionization front. Gas this close to I-fronts typically has a low photo-ionization rate (Nasir & D’Aloisio 2020) and/or is un-relaxed (Park

⁷ These probes include Ly α/β forest statistics from QSO spectra (Fan et al. 2006; Becker et al. 2015; McGreer et al. 2015; Bosman et al. 2021; Zhu et al. 2021, 2022), the mean free path (Worseck et al. 2014; Becker et al. 2021;

Bosman 2021), and the LAE-forest connection (Becker et al. 2018; Meyer et al. 2020; Christenson et al. 2021; Ishimoto et al. 2022).

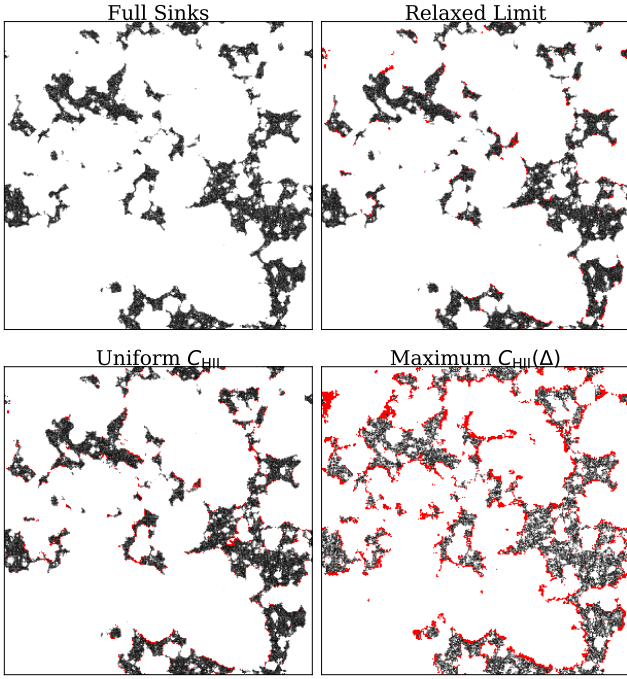


Figure 6. Visualization of neutral islands at 10% volume neutral fraction for our sinks models, assuming our fiducial source scenario. To aid comparison, the red shading highlights neutral regions that are ionized in the Full Sinks model. The Full Sinks, Relaxed Limit and Uniform C_{HI} models have visually similar island morphologies, while the Maximum $C_{\text{HI}}(\Delta)$ case has more extended and more fragmented islands.

et al. 2016; D’Aloisio et al. 2020) and is thus likely to be opaque to both LyC and Ly α photons.

Figure 7 shows the NISD at 10% volume neutral fraction for our sinks models (which occurs at $z \approx 5.6$ for all models except the Maximum $C_{\text{HI}}(\Delta)$ case, which is shown at $z \approx 6.6$). The Maximum $C_{\text{HI}}(\Delta)$ model has the smallest islands while the other models are all very similar. The average island sizes for the Relaxed Limit, Full Sinks, Uniform C_{HI} and Maximum $C_{\text{HI}}(\Delta)$ models are $7.5 h^{-1}\text{Mpc}$, $7.9 h^{-1}\text{Mpc}$, $7.5 h^{-1}\text{Mpc}$, and $6.1 h^{-1}\text{Mpc}$, respectively. In spite of the Maximum $C_{\text{HI}}(\Delta)$ model having more spatially extended neutral structures, the large abundance of small ionized bubbles within these structures break them up and shift the NISD towards smaller sizes. We see that even the approximation of a fully pressure-smoothed IGM is likely acceptable for capturing the morphology of neutral islands. On the other hand, ignoring pressure smoothing effects leads to a $\approx 20\%$ under-estimate of the mean island size in our fiducial source model.

4 INTERPLAY BETWEEN SOURCES AND SINKS

4.1 Source Models

In this section, we will generalize our analysis to include different models for the sources. Most previous studies of morphology have varied the source and sinks properties one at a time, while keeping the other fixed (e.g. McQuinn et al. 2007; Shukla et al. 2016; Mao et al. 2020; Giri et al. 2019a; Wu et al. 2022; Chen et al. 2022). Our use of efficient RT simulations with sink dynamics included allows us to explore the relationship between the sources and sinks as it pertains to morphology. We consider three models for the sources:

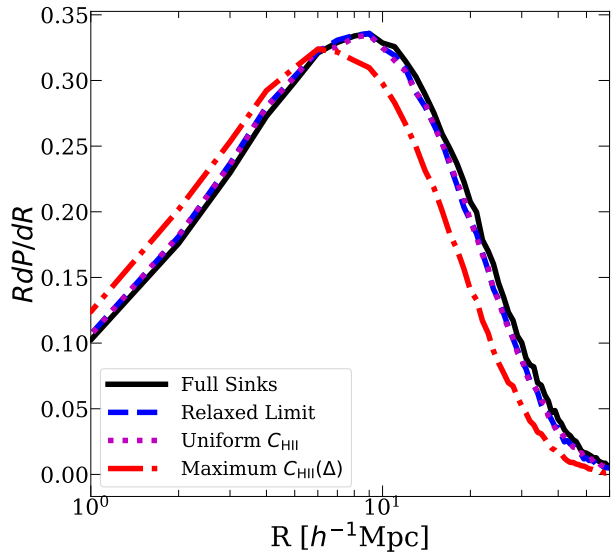


Figure 7. Neutral island size distribution defined such that any cell with $x_{\text{HI}} > 0.01$ is part of an island. We include all the sinks models in Figure 5 and adopt our fiducial source model. The Maximum $C_{\text{HI}}(\Delta)$ model has smaller islands, while the NISDs for the other three models are all very similar.

- **Democratic Sources:** This model differs from our fiducial model in that it assigns all halos the same ionizing emissivity independent of their luminosity, i.e. $\beta = 0$ (see §2.4). At $z = 6$, 50% of the ionizing emissivity is produced by halos in the mass range $10^9 < M/[h^{-1} M_\odot] < 1.8 \times 10^9$ ($-12.6 > M_{\text{UV}} > -13.4$). This model was introduced in Cain et al. (2021) in an attempt to find a model that better recovers the short mean free path at $z = 6$ reported by Becker et al. (2021). This kind of picture would require a steep dependence of f_{esc} and/or the ionizing efficiency ξ_{ion} on luminosity, specifically, $f_{\text{esc}}\xi_{\text{ion}} \propto L_{\text{UV}}^{-1}$ (corresponding to roughly $f_{\text{esc}}\xi_{\text{ion}} \propto M^{-1.4}$ over most of the mass range at $z = 6$). The sources driving reionization in this model are almost entirely below current detection limits, in contrast to the Oligarchic Sources model described below.

- **Fiducial Sources:** Our fiducial scenario with $M_{\min} = 10^9 h^{-1} M_\odot$ and with the emissivity of each halo proportional to its UV luminosity (i.e. $\beta = 1$). At $z = 6$, halos with masses in the range $10^9 < M/[h^{-1} M_\odot] < 1.8 \times 10^{10}$ ($-12.6 < M_{\text{UV}} < -16.9$) contribute 50% of the ionizing emissivity. Of our three source models, this one is most similar to parameterizations commonly used in simulations, e.g. those that assume the emissivity to be proportional to halo mass (Mao et al. 2020; Keating et al. 2020a,b; Bianco et al. 2021).

- **Oligarchic Sources:** In this model, bright and massive sources – the “oligarchs” – dominate reionization. We adopt $M_{\min} = 2 \times 10^{10} h^{-1} M_\odot$ with $\beta = 1$, corresponding to a limiting magnitude of $M_{\text{UV}}^{\max}(z = 6) \approx -17$, roughly the limit of current observations at $5 < z < 10$ (Finkelstein 2016; Bouwens et al. 2021). Thus it assumes that the sources responsible for reionization have, for the most part, already been observed. This model is qualitatively similar to that proposed by Naidu et al. (2020) (see also Naidu et al. (2022); Matthee et al. (2022)). It also serves to contrast starkly with the Democratic Sources model.

To make some contact with previous works exploring how the source properties affect morphology, Figure 8 shows ionization maps at 50% volume ionized ($z \sim 7$) for our Democratic Sources (left), Fiducial Sources (middle) and Oligarchic Sources (right),

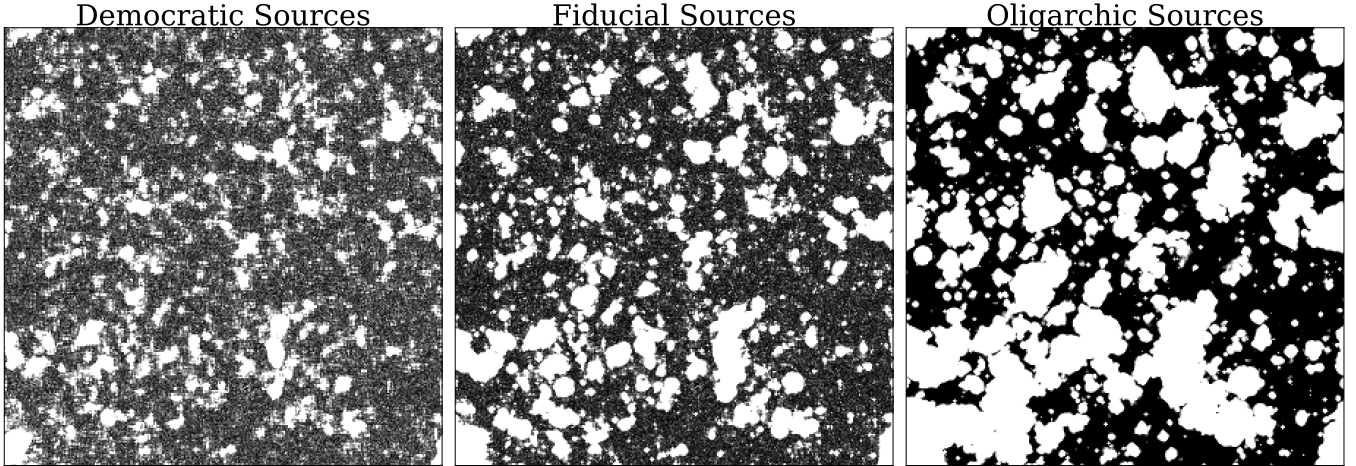


Figure 8. Ionization maps at 50% volume ionized for the Democratic Sources (left), Fiducial (middle) and Oligarchic Sources (right) models, all assuming the Full Sinks model. From left to right, the contribution to the photon budget from the brightest, most massive halos increases. Reionization by more massive, highly biased sources leads to ionized bubbles being larger and fewer in number.

all assuming the Full Sinks model. The differences are clearly visible in the ionization fields; in the models driven by brighter sources, the ionized bubbles are larger and fewer in number. This is because the most massive, rare sources produce a larger fraction of the photons in the Fiducial and Oligarchic Sources models. This familiar result has been observed in many previous studies (e.g. McQuinn et al. 2007; Giri et al. 2019a; Kannan et al. 2022; Chen et al. 2022). Now we turn our attention to the interplay between the sources and sinks.

4.2 Results

Figure 9 shows $\Delta_{21}(k)$ at 20%, 50%, and 80% ionized, in the same format as the bottom panel of Figure 5, for all combinations of source and sinks models. The top and bottom rows show results for the Democratic Sources and Oligarchic Sources models, while the results for the Fiducial Sources model (same as Figure 5) are shown by the thin lines in the bottom row. Note that models sharing the same sinks prescription have similar reionization histories and the same emissivity histories as those shown in Fig. 1. In the Democratic Sources case, the differences between sinks models are smaller at 20% ionized but somewhat larger at 50% and 80% ionized than in the Fiducial Sources case. The suppression of Δ_{21} at $k = 0.1 \text{ } h\text{Mpc}^{-1}$ in the latter half of reionization relative to the Full Sinks case has increased from 25–45% for the Fiducial Sources case to 60–70%. In addition, there are now $\approx 20\%$ differences between the Relaxed Limit, Full Sinks, and Uniform C_{HII} models at 50% ionized. The Uniform C_{HII} model is $\approx 20\%$ below the Full Sinks and Relaxed Limit models at 80% ionized.

It is interesting that for the Democratic Sources model (top row) the Full Sinks and Uniform C_{HII} models have appreciably different Δ_{21} . In particular, the Full Sinks model has *more* large-scale power, which is indicative of larger ionized bubbles. Recall from our discussion in §3.2 that the Full Sinks model should be expected to favor the growth of larger bubbles more than the Uniform C_{HII} case owing to lower (higher) clumping factors in over-dense (under-dense) regions in the former. It seems that these differences, which had little effect on morphology in our Fiducial Sources model, do become important in the limit that very faint,

low-bias sources drive reionization. We caution, however, that this effect may be exaggerated due to our probable over-estimation of the impact of un-relaxed gas, discussed in §2.3.

By contrast, in the Oligarchic Sources case, the differences between the first three models are 10% or less between the Full Sinks, Relaxed Limit, and Uniform C_{HII} models in all of the panels. More strikingly, the Maximum $C_{\text{HII}}(\Delta)$ model actually has *more* large-scale power than the others, likely thanks to its earlier reionization history. At 50% and 80% ionized even the Maximum $C_{\text{HII}}(\Delta)$ model is very similar to the other two⁸. The insensitivity of morphology to the sinks in the Oligarchic Sources model strongly contrasts the much stronger dependence seen in the Democratic Sources model.

Why is morphology sensitive to the sinks in models driven by fainter sources, but not in the Oligarchic Sources scenario? In §3, we saw that sinks limit the sizes of large ionized bubbles. However, it is harder for them to do so in the Oligarchic Sources scenario for two reasons. Nearly all the emissivity is concentrated in highly biased regions, strongly favoring the growth of the largest ionized bubbles. Second, these bubbles grow fast enough to escape the overdensities in which they are born before recombinations begin having a significant impact. This mitigates the “disadvantage” those bubbles have of inhabiting over-dense regions. In these ways, sources in the Oligarchic Sources model “win out” over the sinks in terms of shaping morphology. In the Democratic Sources model, by contrast, the sources are less biased than in Fiducial Sources and the sinks can more easily slow the growth of the largest bubbles. In other words, the sinks are unable to tax the rich enough to affect

⁸ In the Oligarchic Sources scenario, the earlier ionization history in the Maximum $C_{\text{HII}}(\Delta)$ model may obscure morphological differences that would be present if it had the same reionization history as the other sinks models. This is because the bias of the sources evolves strongly with redshift in the Oligarchic Sources model due to its high M_{\min} . To check this, we ran a Relaxed Limit simulation with an accelerated reionization history similar to the Maximum $C_{\text{HII}}(\Delta)$ one. We found evidence for mild suppression (at most 15% at $k = 0.1 \text{ } h\text{Mpc}^{-1}$) at 50% ionized, and no sign of suppression at 80% ionized. This is less than the effect seen in the Fiducial Sources case, confirming our statement in the text.

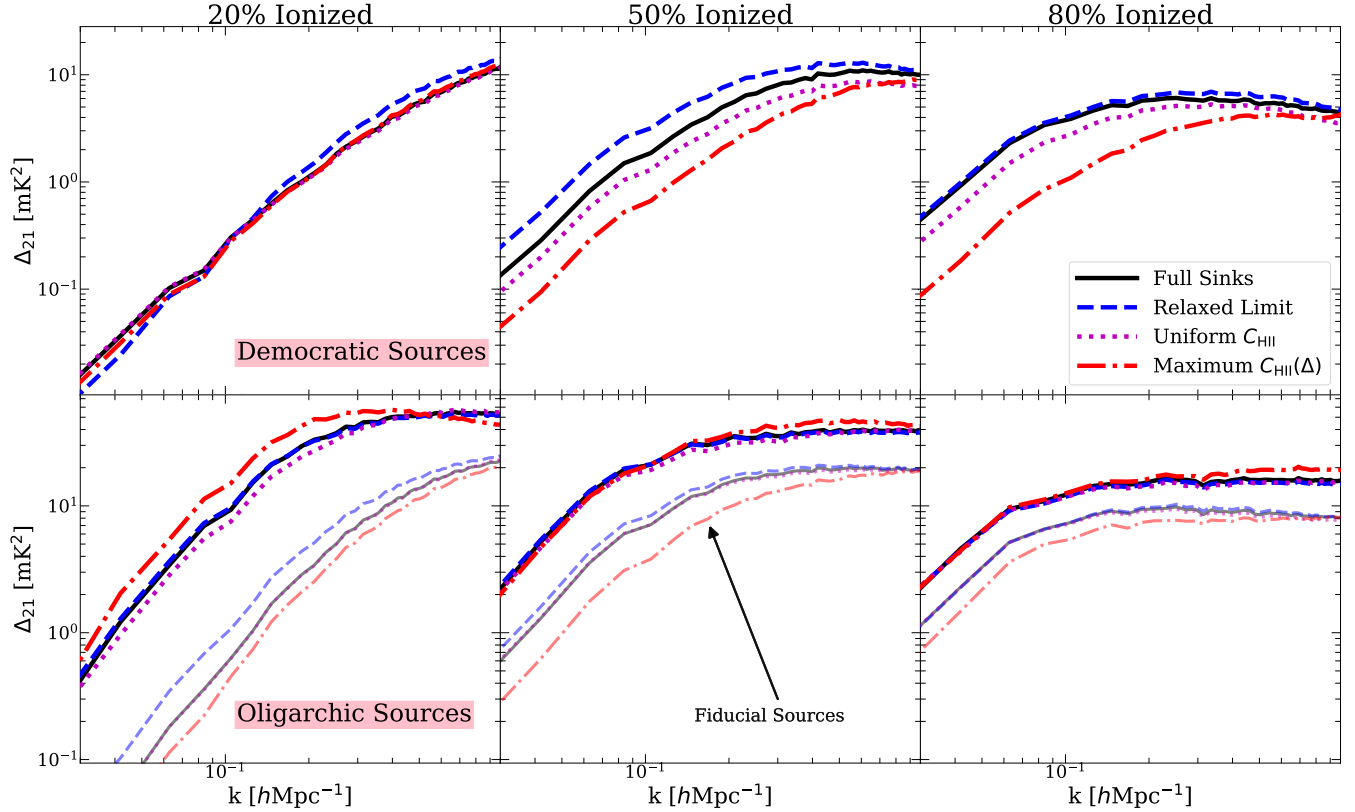


Figure 9. $\Delta_{21}(k)$ for all our sources and sinks models, illustrating the interplay between the sources and sinks of reionization. The top and bottom rows show results for the Democratic Sources and Oligarchic Sources models, respectively. The Fiducial Sources result is shown again by the thin curves in the bottom panel for comparison. The magnitude of the sinks’ effect on morphology clearly depends on the nature of the sources. In the Democratic Sources scenario (top row), the differences between the sinks models are significantly larger than in the Oligarchic Sources scenario. Notably, in the former, the Uniform C_{HII} model no longer matches so well the Full Sinks results, as it did for Fiducial Sources (compare to the thin curves in the bottom row). By contrast, in the Oligarchic Sources scenario, even the Maximum $C_{\text{HII}}(\Delta)$ model matches the others well, especially at 50% and 80% ionization. We are led to conclude that in reionization scenarios driven by less (more) biased sources, the sinks become more (less) important for shaping morphology.

morphology when the source bias is very high, and become more effective at taxing them when the source bias is reduced.

This result has implications for forthcoming efforts to model reionization and interpret observations. Most straightforwardly, it demonstrates that studying the sinks and sources one at a time can produce biased results. For example, studying the sinks in a scenario with only highly biased sources would lead to the incorrect conclusion that they are unimportant for morphology. Another point is that very highly-biased source models may be relatively easy to rule out (or confirm) with forthcoming 21 cm observations from reionization. For example, an upper limit of e.g. $\Delta_{21}(k = 0.1 \text{ hMpc}^{-1}) \leq 10 \text{ mK}^2$ midway through reionization would strongly disfavor the Oligarchic Sources model (which has $\Delta_{21}(k = 0.1 \text{ hMpc}^{-1}) \approx 20 \text{ mK}^2$ at $x_{\text{ion}}^V = 0.5$), since any physically reasonable sinks model would be unable to push Δ_{21} much lower than this⁹. The tightest upper limit to date from HERA (Abdurashidova et al. 2022b) is $\Delta_{21} \leq 946 \text{ mK}^2$ at $z \sim 7.9$ and $k = 0.19 \text{ hMpc}^{-1}$, less than 2 dex away from reaching the prediction of our Oligarchic Sources model. Other probes

that are sensitive to the existence of large ionized regions, such as the visibility of LAEs at $z > 6$ (Vanzella et al. 2011; Jung et al. 2020; Tilvi et al. 2020; Endsley et al. 2021), may also be able to identify large bubbles like those predicted by the Oligarchic Sources model.

5 CONCLUSION

At present, there is no consensus on how much of an effect the sinks had in shaping reionization’s morphology and, relatedly, how important they are for interpreting its observables. We have attempted to address these questions using cosmological RT simulations of reionization. Our simulations include the sub-grid model for the ionizing photon opacity developed by Cain et al. (2021), which is based on high-resolution, fully coupled radiative hydrodynamics simulations of the IGM. The model improves over previous efforts in several key ways: it includes the effects of self-shielding and hydrodynamic response to photo-heating, keeping track of their dependencies on the LyC intensity, the timing of (local) reionization, and the environmental density. Our main conclusions can be summarized as follows:

- The sinks decrease the sizes of the largest ionized bubbles during reionization. We explored this effect in our detailed sub-grid model (Full Sinks), and in 3 other models representative of the ways that sinks have been implemented in previous studies: (1) A model that assumes a pressure-smoothed IGM (Relaxed Limit); (2) A simple

⁹ This statement presumes that at fixed ionized fraction, only the sources and sinks appreciably impact morphology. Two other effects - redshift-space distortions (Ross et al. 2021) and spin temperature fluctuations (Abdurashidova et al. 2022a) may also impact the observed signal significantly. However, both of these work to boost large-scale power, which would only strengthen our statement about upper limits.

clumping factor without dynamics or spatial in-homogeneity, tuned to have the same photon budget as our fiducial model (**Uniform C_{HII}**); (3) An in-homogeneous clumping model from [Mao et al. \(2020\)](#) that neglects pressure smoothing, thus representing a kind of upper limit on the effects of sinks (**Maximum C_{HII}(Δ)**).

- For our fiducial source model, which assumes the same escape fraction and ionizing efficiency for all sources, the **Full Sinks** model has up to $\sim 10 - 20\%$ smaller mean bubble sizes compared to the **Relaxed Limit** model in the first half of reionization. These differences mostly disappear in the second half.

- By contrast, the **Maximum C_{HII}(Δ)** model underestimates bubble sizes by 30–40% (compared to the **Full Sinks** model). Ignoring the dynamical effects of pressure smoothing and photoevaporation can over-estimate significantly the sinks’ effects on morphology.

- We were able to reproduce an almost identical morphology to our **Full Sinks** model using a uniform constant sub-grid clumping factor (the **Uniform C_{HII}** model). Hence, under typical assumptions about reionization’s source population, with regards to morphology, it appears that the detailed dynamics and spatial in-homogeneity of the sinks can be adequately modeled in an average sense with a sub-grid clumping factor. We emphasize, however, that the **Full Sinks** and **Uniform C_{HII}** models exhibit significant differences in Γ_{HI} (Fig. 1), which could render predictions for, e.g., the Ly α forest quite different.

- Differences in bubbles sizes between our models are manifest in the predicted power spectrum of the red-shifted 21cm background. The **Maximum C_{HII}(Δ)** under-estimates the large-scale 21 cm power by 25 – 45% throughout reionization compared to our **Full Sinks** model for our fiducial source prescription. The **Relaxed Limit** model over-estimates power somewhat early in reionization, but becomes similar to both the **Full Sinks** and **Uniform C_{HII}** cases in reionization’s latter half.

- The morphology of neutral islands near the end of reionization is very similar in all of the models except the **Maximum C_{HII}(Δ)** case, which produces smaller islands. The islands in that model are 20% too small on average, highlighting again the importance of including the effects of pressure smoothing.

- The strength of the sinks’ effect on morphology is sensitive to the properties of the sources that drove reionization. In a model where reionization was driven entirely by bright ($M_{UV} < -17$), highly biased galaxies, the sinks suppress the 21 cm power at the 10% level at a fixed ionized fraction throughout reionization, even in the **Maximum C_{HII}(Δ)** case. By contrast, when faint ($M_{UV} \sim -13$), low-bias galaxies drove reionization, the large-scale 21 cm power can be suppressed by up to 70%, and the morphology in the **Full Sinks** and **Uniform C_{HII}** models differ significantly. This result highlights the need to study the effects of sinks and sources together instead of separately. Moreover, the insensitivity of morphology to sinks in highly biased source models makes such models easier targets for forthcoming 21 cm experiments like HERA and SKA, and other probes sensitive to the presence of very large ionized bubbles.

Our **Full Sinks** model can be improved on in several ways. First, in future iterations we plan to address the caveats discussed in §2.3, namely the possible under-counting of rare, massive sinks and double-counting of absorptions in self-shielded systems. These issues can be addressed with sub-grid simulations in larger volumes and by explicitly modeling the evolution of the residual H I fraction in self-shielded systems. A notable uncertainty in our results is that simulations upon which our sub-grid model is based do not include galaxy formation processes, which may affect significantly the structure and state of sinks near massive halos.

Given the interplay between sources and sinks pointed out here, future studies should also move beyond simplistic source parameterizations. Source models should ideally incorporate physically motivated prescriptions for effects such as feedback from reionization ([Shapiro et al. 1994](#); [Thoul & Weinberg 1996](#); [Gnedin 2000](#); [Hoeft et al. 2006](#); [Furlanetto et al. 2011](#); [Wu et al. 2019](#); [Ocvirk et al. 2021](#)), bursty star formation ([Weisz et al. 2011](#); [Emami et al. 2019](#); [Furlanetto & Mirocha 2022](#)), galaxy formation histories ([Bullock et al. 2000](#); [Somerville & Davé 2015](#); [Mirocha et al. 2021](#)), and for fesc ([Kuhlen & Faucher-Giguère 2012](#); [Barrow et al. 2020](#); [Maji et al. 2022](#); [Marques-Chaves et al. 2022](#); [Yeh et al. 2022](#)), all of which play important roles in setting the abundance and bias of the sources.

ACKNOWLEDGEMENTS

We thank Simeon Bird for his help running MP-Gadget, and Hy Trac for providing the SCORCH simulation results against which we calibrated our source models. A.D.’s group is supported by NASA 19-ATP19-0191, NSF AST-2045600, and JWST-AR-02608.001-A. M.M. also acknowledges NASA 19-ATP19-0191 . All computations were made possible by NSF XSEDE allocation TG-PHY210041 and the NASA HEC Program through the NAS Division at Ames Research Center.

REFERENCES

- Abdurashidova Z., et al., 2022a, [ApJ](#), **924**, 51
 Abdurashidova Z., et al., 2022b, [ApJ](#), **925**, 221
 Abel T., Wandelt B. D., 2002, [MNRAS](#), **330**, L53
 Ahn K., Iliev I. T., Shapiro P. R., Srisawat C., 2015, [MNRAS](#), **450**, 1486
 Alvarez M. A., Abel T., 2012, [ApJ](#), **747**, 126
 Barrow K. S. S., Robertson B. E., Ellis R. S., Nakajima K., Saxena A., Stark D. P., Tang M., 2020, [ApJ](#), **902**, L39
 Becker G. D., Bolton J. S., 2013, [MNRAS](#), **436**, 1023
 Becker G. D., Bolton J. S., Madau P., Pettini M., Ryan-Weber E. V., Venemans B. P., 2015, [MNRAS](#), **447**, 3402
 Becker G. D., Davies F. B., Furlanetto S. R., Malkan M. A., Boera E., Douglass C., 2018, [ApJ](#), 863, 92
 Becker G. D., D’Aloisio A., Christenson H. M., Zhu Y., Worseck G., Bolton J. S., 2021, [MNRAS](#), **508**, 1853
 Bianco M., Iliev I. T., Ahn K., Giri S. K., Mao Y., Park H., Shapiro P. R., 2021, [MNRAS](#), **504**, 2443
 Bosman S. E. I., 2021, arXiv e-prints, [p. arXiv:2108.12446](#)
 Bosman S. E. I., Fan X., Jiang L., Reed S., Matsuoka Y., Becker G., Haehnelt M., 2018, [MNRAS](#), **479**, 1055
 Bosman S. E. I., et al., 2021, arXiv e-prints, [p. arXiv:2108.03699](#)
 Bouwens R. J., et al., 2021, [AJ](#), **162**, 47
 Bullock J. S., Kravtsov A. V., Weinberg D. H., 2000, [ApJ](#), **539**, 517
 Cain C., D’Aloisio A., Gangolli N., Becker G. D., 2021, [ApJ](#), **917**, L37
 Calverley A. P., Becker G. D., Haehnelt M. G., Bolton J. S., 2011, [Monthly Notices of the Royal Astronomical Society](#), **412**, 2543
 Chen N., Trac H., Mukherjee S., Cen R., 2022, arXiv e-prints, [p. arXiv:2203.04337](#)
 Choudhury T. R., Paranjape A., Bosman S. E. I., 2021, [MNRAS](#), **501**, 5782
 Christenson H. M., Becker G. D., Furlanetto S. R., Davies F. B., Malkan M. A., Zhu Y., Boera E., Trapp A., 2021, [ApJ](#), **923**, 87
 D’Aloisio A., McQuinn M., Davies F. B., Furlanetto S. R., 2018, [MNRAS](#), **473**, 560
 D’Aloisio A., McQuinn M., Trac H., Cain C., Mesinger A., 2020, [The Astrophysical Journal](#), **898**, 149
 Davies F. B., Furlanetto S. R., 2016, [MNRAS](#), **460**, 1328
 Davies F. B., Furlanetto S. R., 2022, [MNRAS](#), **514**, 1302
 Davies F. B., et al., 2018, [The Astrophysical Journal](#), **864**, 142

- Davies F. B., Bosman S. E. I., Furlanetto S. R., Becker G. D., D'Aloisio A., 2021, *ApJ*, **918**, L35
- DeBoer D. R., et al., 2017, *PASP*, **129**, 045001
- Doré O., et al., 2014, arXiv e-prints, p. [arXiv:1412.4872](https://arxiv.org/abs/1412.4872)
- Eilers A.-C., Davies F. B., Hennawi J. F., 2018, *ApJ*, **864**, 53
- Emami N., Siana B., Weisz D. R., Johnson B. D., Ma X., El-Badry K., 2019, *ApJ*, **881**, 71
- Emberson J. D., Thomas R. M., Alvarez M. A., 2013, *The Astrophysical Journal*, **763**, 146
- Endsley R., Stark D. P., Charlot S., Chevallard J., Robertson B., Bouwens R. J., Stefanon M., 2021, *MNRAS*, **502**, 6044
- Fan X., et al., 2006, *AJ*, **132**, 117
- Feng Y., Bird S., Anderson L., Font-Ribera A., Pedersen C., 2018, MP-Gadget/MP-Gadget: A tag for getting a DOI, doi:10.5281/zenodo.1451799, <https://doi.org/10.5281/zenodo.1451799>
- Finkelstein S. L., 2016, *Publ. Astron. Soc. Australia*, **33**, e037
- Finkelstein S. L., et al., 2019, *ApJ*, **879**, 36
- Finlator K., Davé R., Özel F., 2011, *The Astrophysical Journal*, **743**, 169
- Furlanetto S. R., Mirocha J., 2022, *MNRAS*, **511**, 3895
- Furlanetto S. R., Oh S. P., 2005, *Monthly Notices of the Royal Astronomical Society*, **363**, 1031
- Garaldi E., Kannan R., Smith A., Springel V., Pakmor R., Vogelsberger M., Hernquist L., 2022, *MNRAS*,
- Gazagnes S., Koopmans L. V. E., Wilkinson M. H. F., 2021, *MNRAS*, **502**, 1816
- Giri S. K., Mellema G., Ghara R., 2018, *MNRAS*, **479**, 5596
- Giri S. K., Mellema G., Aldheimer T., Dixon K. L., Iliev I. T., 2019a, *MNRAS*, **489**, 1590
- Giri S. K., D'Aloisio A., Mellema G., Komatsu E., Ghara R., Majumdar S., 2019b, *Journal of Cosmology and Astro-Particle Physics*, **2019**, 058
- Gnedin N. Y., 2000, *ApJ*, **542**, 535
- Gnedin N. Y., 2014, *ApJ*, **793**, 29
- Gnedin N. Y., Kravtsov A. V., Rudd D. H., 2011, *ApJS*, **194**, 46
- Gorski K. M., Wandelt B. D., Hansen F. K., Hivon E., Banday A. J., 1999, arXiv e-prints, pp [astro-ph/9905275](https://arxiv.org/abs/astro-ph/9905275)
- Greig B., Mesinger A., Haiman Z., Simcoe R. A., 2016, *Monthly Notices of the Royal Astronomical Society*, **466**, 4239
- Greig B., Mesinger A., Bañados E., 2019, *MNRAS*, **484**, 5094
- Greig B., Mesinger A., Davies F. B., Wang F., Yang J., Hennawi J. F., 2022, *MNRAS*, **512**, 5390
- Hoeft M., Yepes G., Gottlöber S., Springel V., 2006, *MNRAS*, **371**, 401
- Hu W., et al., 2019, *ApJ*, **886**, 90
- Iliev I. T., Shapiro P. R., Raga A. C., 2005a, *Monthly Notices of the Royal Astronomical Society*, **361**, 405
- Iliev I. T., Scannapieco E., Shapiro P. R., 2005b, *ApJ*, **624**, 491
- Iliev I. T., Mellema G., Ahn K., Shapiro P. R., Mao Y., Pen U.-L., 2014, *MNRAS*, **439**, 725
- Ishimoto R., et al., 2022, arXiv e-prints, p. [arXiv:2207.05098](https://arxiv.org/abs/2207.05098)
- Jung I., et al., 2020, *ApJ*, **904**, 144
- Kannan R., Garaldi E., Smith A., Pakmor R., Springel V., Vogelsberger M., Hernquist L., 2022, *MNRAS*, **511**, 4005
- Kashikawa N., et al., 2006, *ApJ*, **648**, 7
- Kaur H. D., Gillet N., Mesinger A., 2020, *MNRAS*, **495**, 2354
- Keating L. C., Weinberger L. H., Kulkarni G., Haehnelt M. G., Chardin J., Aubert D., 2020a, *MNRAS*, **491**, 1736
- Keating L. C., Kulkarni G., Haehnelt M. G., Chardin J., Aubert D., 2020b, *MNRAS*, **497**, 906
- Koopmans L., et al., 2015, in Advancing Astrophysics with the Square Kilometre Array (AASKA14). p. 1 ([arXiv:1505.07568](https://arxiv.org/abs/1505.07568)), doi:10.22323/1.215.0001
- Kuhlen M., Faucher-Giguère C.-A., 2012, *Monthly Notices of the Royal Astronomical Society*, **423**, 862
- Kulkarni G., Keating L. C., Haehnelt M. G., Bosman S. E. I., Puchwein E., Chardin J., Aubert D., 2019, *MNRAS*, **485**, L24
- Lewis J. S. W., et al., 2020, *MNRAS*, **496**, 4342
- Lewis J. S. W., et al., 2022, arXiv e-prints, p. [arXiv:2202.05869](https://arxiv.org/abs/2202.05869)
- Maji M., et al., 2022, *A&A*, **663**, A66
- Malloy M., Lidz A., 2015, *ApJ*, **799**, 179
- Mao Y., Koda J., Shapiro P. R., Iliev I. T., Mellema G., Park H., Ahn K., Bianco M., 2020, *MNRAS*, **491**, 1600
- Marques-Chaves R., et al., 2022, *A&A*, **663**, L1
- Mason C. A., et al., 2018, *ApJ*, **857**, L11
- Mason C. A., et al., 2019, *Monthly Notices of the Royal Astronomical Society*, **485**, 3947
- Matthee J., et al., 2022, *MNRAS*,
- McGreer I. D., Mesinger A., D'Odorico V., 2015, *MNRAS*, **447**, 499
- McQuinn M., D'Aloisio A., 2018, *JCAP*, **2018**, 016
- McQuinn M., Lidz A., Zahn O., Dutta S., Hernquist L., Zaldarriaga M., 2007, *MNRAS*, **377**, 1043
- McQuinn M., Oh S. P., Faucher-Giguère C.-A., 2011, *The Astrophysical Journal*, **743**, 82
- Mellema G., et al., 2013, *Experimental Astronomy*, **36**, 235
- Mesinger A., Furlanetto S., 2007, *ApJ*, **669**, 663
- Mesinger A., Aykutalp A., Vanzella E., Pentericci L., Ferrara A., Dijkstra M., 2015, *MNRAS*, **446**, 566
- Meyer R. A., et al., 2020, *MNRAS*, **494**, 1560
- Mirocha J., Plante P. L., Liu A., 2021, *Monthly Notices of the Royal Astronomical Society*, **507**, 3872
- Mortlock D. J., et al., 2011, *Nature*, **474**, 616
- Naidu R. P., Tacchella S., Mason C. A., Bose S., Oesch P. A., Conroy C., 2020, *ApJ*, **892**, 109
- Naidu R. P., et al., 2022, *MNRAS*, **510**, 4582
- Naoz S., Barkana R., 2007, *MNRAS*, **377**, 667
- Nasir F., D'Aloisio A., 2020, *Monthly Notices of the Royal Astronomical Society*, **494**, 3080–3094
- Nasir F., Cain C., D'Aloisio A., Gangolfi N., McQuinn M., 2021, *ApJ*, **923**, 161
- Ocvirk P., et al., 2016, *MNRAS*, **463**, 1462
- Ocvirk P., Lewis J. S. W., Gillet N., Chardin J., Aubert D., Deparis N., Thélie É., 2021, *MNRAS*, **507**, 6108
- Ono Y., et al., 2011, *The Astrophysical Journal*, **744**, 83
- Ouchi M., et al., 2018, *PASJ*, **70**, S13
- Park H., Shapiro P. R., Choi J.-h., Yoshida N., Hirano S., Ahn K., 2016, *ApJ*, **831**, 86
- Parsons A. R., et al., 2010, *AJ*, **139**, 1468
- Pentericci L., et al., 2014, *The Astrophysical Journal*, **793**, 113
- Planck Collaboration et al., 2020, *A&A*, **641**, A6
- Qin Y., Mesinger A., Bosman S. E. I., Viel M., 2021, *MNRAS*, **506**, 2390
- Robertson B. E., Ellis R. S., Furlanetto S. R., Dunlop J. S., 2015, *ApJ*, **802**, L19
- Ross H. E., Giri S. K., Mellema G., Dixon K. L., Ghara R., Iliev I. T., 2021, *MNRAS*, **506**, 3717
- Schenker M. A., Stark D. P., Ellis R. S., Robertson B. E., Dunlop J. S., McLure R. J., Kneib J.-P., Richard J., 2012, *ApJ*, **744**, 179
- Shapiro P. R., Giroux M. L., Babul A., 1994, *ApJ*, **427**, 25
- Shapiro P. R., Iliev I. T., Raga A. C., 2004, *Monthly Notices of the Royal Astronomical Society*, **348**, 753
- Shukla H., Mellema G., Iliev I. T., Shapiro P. R., 2016, *MNRAS*, **458**, 135
- Sobacchi E., Mesinger A., 2014, *MNRAS*, **440**, 1662
- Somerville R. S., Davé R., 2015, *ARA&A*, **53**, 51
- Thoul A. A., Weinberg D. H., 1996, *The Astrophysical Journal*, **465**, 608
- Tilvi V., et al., 2020, *ApJ*, **891**, L10
- Tingay S. J., et al., 2013, *Publ. Astron. Soc. Australia*, **30**, e007
- Trac H., Cen R., 2007, *The Astrophysical Journal*, **671**, 1
- Trac H., Pen U.-L., 2004, *New Astron.*, **9**, 443
- Trac H., Cen R., Mansfield P., 2015, *ApJ*, **813**, 54
- Trac H., Chen N., Holst I., Alvarez M. A., Cen R., 2022, *ApJ*, **927**, 186
- Vanzella E., et al., 2011, *ApJ*, **730**, L35
- Wang F., et al., 2020, *ApJ*, **896**, 23
- Watson W. A., Iliev I. T., D'Aloisio A., Knebe A., Shapiro P. R., Yepes G., 2013, *MNRAS*, **433**, 1230
- Weisz D. R., et al., 2011, *The Astrophysical Journal*, **744**, 44
- Worseck G., et al., 2014, *MNRAS*, **445**, 1745
- Wu X., Kannan R., Marinacci F., Vogelsberger M., Hernquist L., 2019, *MNRAS*, **488**, 419

- Wu P.-J., Xu Y., Zhang X., Chen X., 2022, *ApJ*, **927**, 5
 Wyithe J. S. B., Bolton J. S., 2011, *Monthly Notices of the Royal Astronomical Society*, **412**, 1926
 Xu Y., Yue B., Su M., Fan Z., Chen X., 2014, *ApJ*, **781**, 97
 Xu Y., Yue B., Chen X., 2017, *IAU Symp.*, **333**, 64
 Yang J., et al., 2020, *ApJ*, **897**, L14
 Yatawatta S., et al., 2013, *A&A*, **550**, A136
 Yeh J. Y. C., et al., 2022, arXiv e-prints, p. arXiv:2205.02238
 Zhu Y., et al., 2021, *ApJ*, **923**, 223
 Zhu Y., et al., 2022, *ApJ*, **932**, 76

APPENDIX A: NUMERICAL CONVERGENCE

Here we describe some additional parameters in our code and demonstrate convergence of the ionization field in our simulations. The first parameter is N_{iter} , the number of times Eq. 1 is iterated with the equation for $\bar{\lambda}$ (Eq. 3 or 4) during each time step. Our fiducial value is $N_{\text{iter}} = 5$. Our initial guess for Γ_{HI} assumes $\bar{\lambda} \gg \Delta x_{\text{cell}}$, where Δx_{cell} is the cell size, in which limit Eq. 1 is independent of $\bar{\lambda}$. Thus in general, convergence takes longest when $\bar{\lambda} \lesssim \Delta x_{\text{cell}}$ - that is, in optically thick cells. To test convergence of N_{iter} , we ran simulations with $N_{\text{iter}} = 1, 3, 5$, and 10 on a coarse-grained ($N = 150^3$) version of our reionization volume using the Democratic Sources and Uniform CH_{II} models. In Fig. A1 we show $\Delta_{21}(k)$ vs. wavenumber at 30% and 70% ionized for our tests. The dependence on N_{iter} is greatest at 30% ionized, but becomes less significant at 70% ionized when most ionized cells have $\bar{\lambda} > 2 h^{-1}\text{Mpc}$. Even at 30% ionized, the fiducial $N_{\text{iter}} = 5$ case never deviates by more than 10% from the $N_{\text{iter}} = 10$ one, demonstrating convergence. Note that this result is conservative because the condition $\bar{\lambda} \lesssim \Delta x_{\text{cell}}$ is more likely to occur for $\Delta x_{\text{cell}} = 2 h^{-1}\text{Mpc}$ than for our fiducial $\Delta x_{\text{cell}} = 1 h^{-1}\text{Mpc}$.

Next we checked for convergence in the angular resolution of the radiation field. This is adjustable in our code through two parameters that control how rays are merged. The first, l_{hpx} , is the order of the HealPix sphere onto which rays are binned when they are merged. Our fiducial $l_{\text{hpx}} = 0$ corresponds to keeping track of 12 directions. The other parameter is N_{ex} - the number of rays per cell that are “exempt” from being merged. Before rays merged, they are sorted in order of their photon counts, and the top $N_{\text{ex}}N^3$ rays are not considered for merging¹⁰. Using the same coarse-grained setup, we checked all combinations of $l_{\text{hpx}} = 0$ and 1 (which corresponds to tracking 48 directions) and $N_{\text{ex}} = 16$ (our fiducial choice) and 44. We found that Δ_{21} for these tests (not shown) to be indistinguishable for all combinations of these parameters on scales of interest, despite the amount of noise in the radiation field decreasing considerably for higher resolution runs.

APPENDIX B: DERIVATION OF EQ. 1 (FOR Γ_{HI})

Here we will derive Eq. 1 for Γ_{HI} . Consider cell i with ionized fraction x_{ion}^i and volume V_{cell} . If the I-front in cell i is infinitely sharp and travels along one axis, then ray j intersecting cell i will travel a distance $x_{\text{ion}}^i \Delta s^{ij}$ (recall Δs^{ij} is the total path length of ray j through cell i) before reaching neutral gas. The number of photons absorbed over this distance is

$$N_{\text{abs}}^i = \sum_{j=1}^{N_{\text{rays}}} N_0^{ij} \left(1 - \exp \left[\frac{-x_{\text{ion}}^i \Delta s^{ij}}{\bar{\lambda}} \right] \right) \quad (\text{B1})$$

¹⁰ We found that this procedure considerably reduces noise in the radiation field, particularly around the brightest sources.

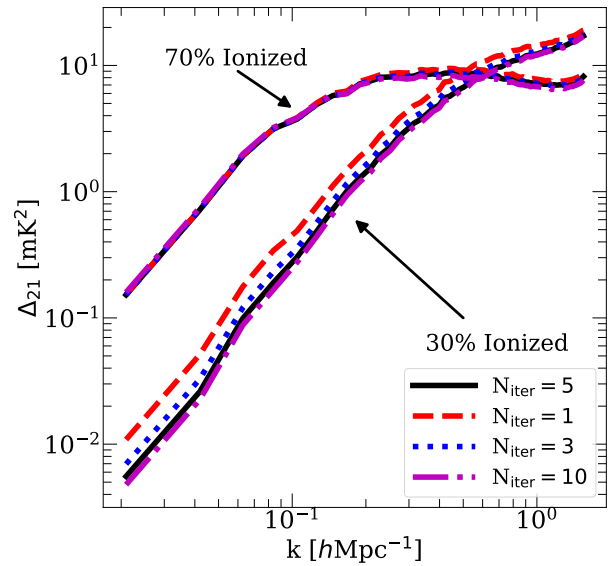


Figure A1. $\Delta_{21}(k)$ at 30% and 70% ionized (see annotations) for four values of N_{iter} (see legend). This test uses the Democratic Sources and Uniform CH_{II} models in a coarse-grained version of the original simulation volume with $2 h^{-1}\text{Mpc}$ cells. Our fiducial value of $N_{\text{iter}} = 5$ is within 10% of the $N_{\text{iter}} = 10$ case at both ionized fractions and at all k , demonstrating convergence.

where N_0^{ij} is the number of photons in ray j entering cell i and $\bar{\lambda}$ is the mean free path in cell i behind the I-front. During a time step Δt , Γ_{HI} behind the I-front is

$$\Gamma_{\text{HI}}^i = \frac{\# \text{ of photons absorbed per time}}{\# \text{ of HI atoms in ionized gas}} = \frac{N_{\text{abs}}^i / \Delta t}{n_{\text{HI}}^i x_{\text{ion}}^i V_{\text{cell}}} \quad (\text{B2})$$

where $x_{\text{ion}}^i V_{\text{cell}}$ is the ionized volume of cell i and

$$n_{\text{HI}}^{\Gamma} \equiv \frac{\langle \Gamma_{\text{HI}} n_{\text{HI}} \rangle_V}{\langle \Gamma_{\text{HI}} \rangle_V} \quad (\text{B3})$$

is the Γ_{HI} -weighted HI number density (the V sub-script denotes a volume average). Eq. 2 relates the numerator of Eq. B3 to our definition for $\bar{\lambda}$ for the small-volume simulations (derived in the next section). Combining Eqs. 2, B3, and B1 yields

$$\Gamma_{\text{HI}}^i = \sum_{j=1}^{N_{\text{rays}}} \frac{N_0^{ij} \left(1 - \exp \left[-x_{\text{ion}}^i \Delta s^{ij} / \bar{\lambda} \right] \right)}{(\bar{\lambda} F_{\gamma} / \langle \Gamma_{\text{HI}} \rangle_V) x_{\text{ion}}^i V_{\text{cell}} \Delta t} \quad (\text{B4})$$

where $F_{\gamma} \equiv \Gamma_{\text{HI}}^0 \bar{\sigma}_{\text{HI}}^{-1}$ is the ionizing flux at the source planes in the small-volume simulations and Γ_{HI}^0 is the photo-ionization rate at the source planes. Because the domain size ($32 h^{-1}\text{kpc}$) is much less than $\bar{\lambda}$ in all our small-volume simulations, F_{γ} usually attenuates very little over the domain width except around self-shielded systems, which (typically) occupy a small fraction of the volume. Thus, $\langle \Gamma_{\text{HI}} \rangle_V \approx \Gamma_{\text{HI}}^0$, which gives

$$\Gamma_{\text{HI}}^i \approx \sum_{j=1}^{N_{\text{rays}}} \frac{N_0^{ij} \left(1 - \exp \left[-x_{\text{ion}}^i \Delta s^{ij} / \bar{\lambda} \right] \right)}{(\bar{\lambda} \bar{\sigma}_{\text{HI}})^{-1} x_{\text{ion}}^i V_{\text{cell}} \Delta t} \quad (\text{B5})$$

which is equivalent to Eq. 1.

Note that Eq. B2 and Eq. B5 together imply that $n_{\text{HI}}^{\Gamma} \approx (\bar{\lambda} \bar{\sigma}_{\text{HI}})^{-1}$ should be true in our small-volume simulations. Figure B1 tests this equality for simulations with $\Gamma_{-12} = 3.0$ (blue curves), 0.3 (red)

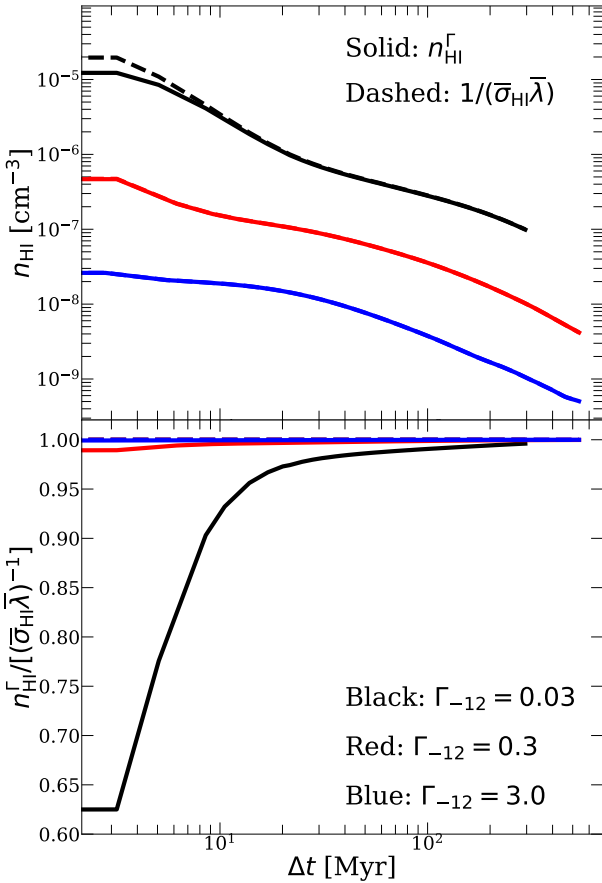


Figure B1. Test of the relation $n_{\text{HI}}^{\Gamma} = (\bar{\lambda}\bar{\sigma}_{\text{HI}})^{-1}$, as required by Eq. 1. **Top:** n_{HI}^{Γ} (solid) and $(\bar{\lambda}\bar{\sigma}_{\text{HI}})^{-1}$ (dashed) vs. time since ionization for small-volume simulations with $\Gamma_{-12} = 3.0$ (blue), 0.3 (red), and 0.03 (black), assuming $z_{\text{re}} = 8$ and $\delta/\sigma = 0$. **Bottom:** the ratio between these two quantities for each case. For $\Gamma_{-12} = 3.0$ and 0.3 the equality holds within a few percent at all times, but for 0.03 agreement to within 10% is not reached until $\Delta t \approx 10$ Myr. This leads to an over-estimate of the absorption rate in recently ionized cells with low Γ_{HI} in our reionization simulations.

and 0.03 (black) for $z_{\text{re}} = 8$ and $\delta/\sigma = 0$ (mean density). The top panel plots both quantities vs. time since ionization, while the bottom panel shows their ratio. In the simulations with $\Gamma_{-12} = 3.0$ and 0.3 the equality holds to within a few percent even during the first few Myr when self-shielding is most important. However in the 0.03 case, they do not agree to within 10% until ≈ 10 Myr after ionization. In the case that $n_{\text{HI}}^{\Gamma} < (\bar{\lambda}\bar{\sigma}_{\text{HI}})^{-1}$, Eq. 1 over-estimates the number of absorptions in ionized gas because it under-estimates Γ_{HI} , and therefore the converged value of $\bar{\lambda}$ (Eq. 3). This means that the opacity is somewhat too high in recently ionized gas with low Γ_{HI} in our reionization simulations. Since these are also the conditions in which gas is usually un-relaxed, this effect adds to the over-estimation of the opacity of un-relaxed gas discussed in §2.3. Note, however, that the test described at the end of that section also brackets this issue, since $\langle \Gamma_{\text{HI}} \rangle_V < \Gamma_{\text{HI}}^0$ yields an under-estimate of C_R and an over-estimate of the $\bar{\lambda}$ derived from it. This suggests that our conclusions about the magnitude of the effect in that section should hold.

APPENDIX C: DERIVATION OF EQ.2 (FOR $\bar{\lambda}$)

In this section we derive our estimator for the frequency-averaged mean free path in our small-volume simulations, $\bar{\lambda}$ (Eq. 2). Let I_{ν} be the specific intensity at the source planes. The ionizing flux along one direction of our box is,

$$F_{\gamma} = \int_{\nu_{\text{HI}}}^{4\nu_{\text{HI}}} \frac{I_{\nu}}{h_p \nu} d\nu, \quad (\text{C1})$$

where h_p is Planck's constant and $h_p \nu_{\text{HI}}$ is the ionization potential of hydrogen. Assuming the radiation streams along the x_1 direction, the photoionization rate at location $\mathbf{x} = (x_1, x_2, x_3)$ along a ray is

$$\Gamma_{\text{HI}}(\mathbf{x}) = \int_{\nu_{\text{HI}}}^{4\nu_{\text{HI}}} \frac{\sigma_{\nu}}{h\nu} I_{\nu} e^{-\int_0^{x_1} dx' n_{\text{HI}}(x', x_2, x_3) \sigma_{\nu}} d\nu, \quad (\text{C2})$$

where $n_{\text{HI}}(\mathbf{x})$ is the proper hydrogen number density and σ_{ν} is its photoionization cross section. We can write

$$\begin{aligned} n_{\text{HI}}(\mathbf{x}) \Gamma_{\text{HI}}(\mathbf{x}) &= \int_{\nu_{\text{HI}}}^{4\nu_{\text{HI}}} d\nu \frac{I_{\nu}}{h\nu} n_{\text{HI}}(\mathbf{x}) \sigma_{\nu} e^{-\int_0^{x_1} dx' n_{\text{HI}}(x', x_2, x_3) \sigma_{\nu}} = \\ &- \int_{\nu_{\text{HI}}}^{4\nu_{\text{HI}}} d\nu \frac{I_{\nu}}{h\nu} \frac{\partial}{\partial x_1} e^{-\int_0^{x_1} dx' n_{\text{HI}}(x', x_2, x_3) \sigma_{\nu}} \end{aligned} \quad (\text{C3})$$

Integrating over the domain volume $V_d = L_d^3$, we obtain

$$V_d \langle n_{\text{HI}} \Gamma_{\text{HI}} \rangle_{V_d} =$$

$$\int_{\nu_{\text{HI}}}^{4\nu_{\text{HI}}} d\nu \frac{I_{\nu}}{h\nu} \int_0^{L_d} dx_2 dx_3 \left(1 - e^{-\int_0^{L_d} dx' n_{\text{HI}}(x', x_2, x_3) \sigma_{\nu}} \right) \quad (\text{C4})$$

where $\langle \dots \rangle_{V_d}$ denotes an average over the domain volume. We define the effective optical depth through

$$e^{-\tau_{\text{eff}}} \equiv \langle e^{-\int_0^{L_d} dx' n_{\text{HI}}(x', x_2, x_3) \sigma_{\nu}} \rangle_{A_d} =$$

$$A_d^{-1} \int_0^{L_d} dx_2 dx_3 e^{-\int_0^{L_d} dx' n_{\text{HI}}(x', x_2, x_3) \sigma_{\nu}} \quad (\text{C5})$$

where $A_d = L_d^2$ and $\langle \dots \rangle_{A_d}$ denotes an average over the transverse plane. Plugging this into equation C4 yields

$$L_d \langle n_{\text{HI}} \Gamma_{\text{HI}} \rangle_{V_d} = \int_{\nu_{\text{HI}}}^{4\nu_{\text{HI}}} d\nu \frac{I_{\nu}}{h\nu} (1 - e^{-\tau_{\text{eff}}}). \quad (\text{C6})$$

The mean free path is defined to be $\bar{\lambda} = L_d/\tau_{\text{eff}}$. Assuming that $\lambda \gg L_d$ (recall that $L_d = 32 h^{-1}$ kpc), we can expand the exponential in equation C6 to first order, yielding

$$\bar{\lambda}^{-1} \equiv \langle \lambda^{-1} \rangle_{\nu} = \frac{\langle n_{\text{HI}} \Gamma_{\text{HI}} \rangle_{V_d}}{F_{\gamma}}, \quad (\text{C7})$$

where we have used that $\langle \lambda^{-1} \rangle_{\nu} = (1/F_{\gamma}) \int_{\nu_{\text{HI}}}^{4\nu_{\text{HI}}} d\nu \frac{I_{\nu}}{h\nu} \lambda^{-1}$. The RHS of Eq. C7 is the volume-averaged absorption rate divided by the incident flux, and is equivalent to the volume averaged absorption coefficient. Note that Eq. C7 counts all absorptions within ionized regions, not just those balanced by recombinations.

APPENDIX D: TEST OF EQ. 3 (TO ACCOUNT FOR EVOLVING Γ_{HI})

In this section we will show how Eq. 3 accounts for the sensitivity of $\bar{\lambda}$ to the history of Γ_{HI} in our RT cells. Figure D1 shows $\bar{\lambda}$

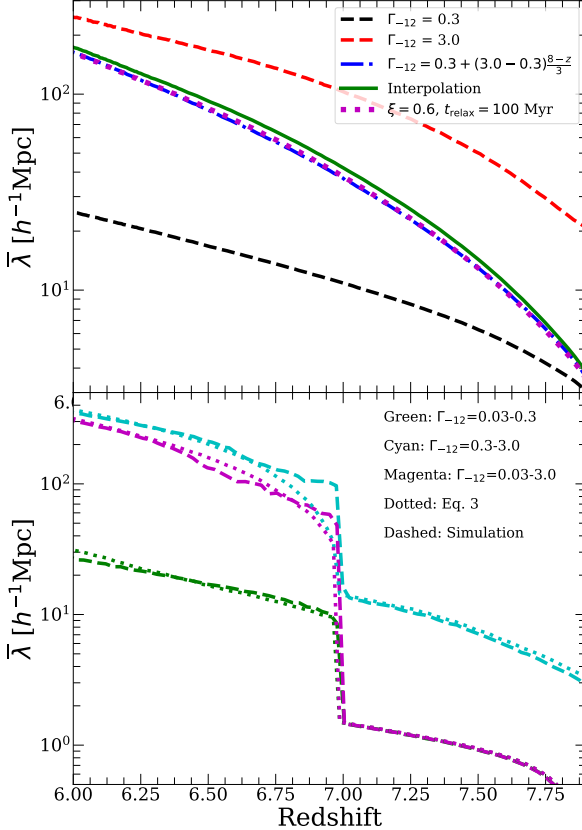


Figure D1. Tests of Eq. 3 using small-volume simulations with evolving Γ_{HI} . **Top:** Test with $\Gamma_{\text{HI}}(z) = 0.3 + (3.0 - 0.3)^{\frac{8-z}{3}}$ (blue dot-dashed) alongside a direct interpolation between simulations with constant Γ_{HI} (green solid) and the result of evaluating Eq. 3 with $\xi = 0.6$ and $t_{\text{relax}} = 100 \text{ Myr}$ (magenta dotted). The interpolation over-estimates $\bar{\lambda}$ by 10–15% while Eq. 3 produces agreement to within a few percent. **Bottom:** Tests in smaller ($0.256 h^{-1}\text{Mpc}$) volumes in which we impulsively increased Γ_{HI} by 1–2 orders of magnitude at $z = 7$. The dashed curves are the simulation results and the dotted curves are Eq. 3. The model agrees reasonably well even in these extreme cases, although the values of ξ and t_{relax} vary between fits (and from our fiducial values).

Starting Γ_{-12}	Ending Γ_{-12}	ξ	$t_{\text{relax}} [\text{Myr}]$
0.03	0.3	0.8	700
0.3	3.0	0.33	100
0.03	3.0	0.67	300

Table D1. Best-fit parameters for our “impulsive- Γ_{HI} ” tests of Eq. 3, shown in Figure D1.

for several tests of Eq. 3 in small-volume simulations with evolving Γ_{HI} . In the top panel, we show the mean free path for a fiducial box size/resolution simulation with $\Gamma_{-12}(z) = 0.3 + (3.0 - 0.3)^{\frac{8-z}{3}}$ (dashed blue curve) alongside two approximations based on constant- Γ_{HI} simulations. The solid green curve is a direct power law interpolation between $\Gamma_{-12} = 3.0$ (red dashed curve) and 0.3 (black dashed curve) simulations. The magenta dotted curve is the result of evaluating Eq. 3 with $\xi = 0.6$ and $t_{\text{relax}} = 100 \text{ Myr}$ (close to our fiducial values for these parameters). We see that the direct interpolation over-estimates $\bar{\lambda}$ by 10–15%, while Eq. 3 agrees with the evolving Γ_{HI} simulation to within a few percent.

We also ran several tests (in smaller boxes) in which we increased Γ_{HI} impulsively by 1–2 orders of magnitude midway through the simulation. These tests represent a “maximum stress test” of Eq. 3, since in reality Γ_{HI} will evolve more gradually. The bottom panel of Fig. D1 shows the result of three tests, with Γ_{HI} impulsively jumping between the values quoted in the legend at $z = 7$. The dashed lines show the simulation results and the dotted lines the result of Eq. 3 (evaluated using a suite of similar simulations with constant Γ_{-12}). Though the values of ξ and t_{relax} that gave these fits, given in Table D1, are somewhat different from each other (and our fiducial model), the goodness of the fits demonstrates the ability of Eq. 3 to capture $\bar{\lambda}$ in a variety of environments accurately. The variation may be due in part to the smaller box sizes of these tests and the fact that ξ and t_{relax} are partially degenerate, but we also do expect that ξ and t_{relax} should in general depend on Γ_{HI} (and, in principle, over-density and z_{reion}). Future work will be required to address the environmental dependence of ξ and t_{relax} in more detail.

This paper has been typeset from a $\text{TeX}/\text{L}\ddot{\text{A}}\text{T}\text{E}\text{X}$ file prepared by the author.